

Study of the $\eta\pi^0$ spectrum and search for a $J^{PC}=1^{-+}$ exotic meson

A. R. Dzierba, J. Gunter, S. Ichiriu, R. Lindenbusch, E. Scott, P. Smith, M. R. Shepherd, and S. Teige
Department of Physics, Indiana University, Bloomington, Indiana 47405

M. Swat and A. P. Szczepaniak
Nuclear Theory Center, Indiana University, Bloomington, Indiana 47405

S. P. Denisov, A. V. Popov, and D. I. Ryabchikov
Institute for High Energy Physics, Protvino, Russian Federation 142284

L. I. Sarycheva
Institute for Nuclear Physics, Moscow, Russian Federation 119899

J. Napolitano
Department of Physics, Rensselaer Polytechnic Institute, Troy, New York 12180

(Received 23 August 2002; published 21 May 2003)

A partial wave analysis (PWA) of the $\eta\pi^0$ system (where $\eta \rightarrow \gamma\gamma$) produced in the charge exchange reaction $\pi^- p \rightarrow \eta\pi^0 n$ at an incident momentum of 18 GeV/c is presented as a function of the $\eta\pi^0$ invariant mass $m_{\eta\pi^0}$ and momentum transfer squared $t_{\pi^- \rightarrow \eta\pi^0}$, from the incident π^- to the outgoing $\eta\pi^0$ system. S , P , and D waves were included in the PWA. The $a_0(980)$, and $a_2(1320)$ states are clearly observed in the overall $\eta\pi^0$ effective mass distribution as well as in the amplitudes associated with S wave and D waves, respectively, after partial wave decomposition. The observed distributions in moments (averages of spherical harmonics) were compared to the results from the PWA and the two are consistent. The distribution in $t_{\pi^- \rightarrow \eta\pi^0}$ for individual D waves associated with natural and unnatural parity exchange in the t channel are consistent with Regge phenomenology. Of particular interest in this study is the P wave since this leads to an exotic $J^{PC}=1^{-+}$ for the $\eta\pi$ system. A P wave is present in the data; however, attempts to describe the mass dependence of the amplitude and phase motion with respect to the D wave as a Breit-Wigner resonance are problematic. This has implications regarding the existence of a reported exotic $J^{PC}=1^{-+}$ meson decaying into $\eta\pi^0$ with a mass near 1.4 GeV/c².

DOI: 10.1103/PhysRevD.67.094015

PACS number(s): 13.25.Jx, 11.55.Jy, 11.80.Et, 14.40.Cs

I. INTRODUCTION

The observation nearly four decades ago that mesons are grouped in nonets, each characterized by unique values of J^{PC} —spin (J), parity (P), and charge conjugation (C) quantum numbers—led to the development of the quark model. Within this picture, mesons are bound states of a quark (q) and antiquark (\bar{q}). The three light-quark flavors (up, down, and strange) suffice to explain the spectroscopy of most—but not all—of the lighter-mass mesons (i.e., below 3 GeV/c²) that do not explicitly carry heavy flavors (charm or flavored quarks). Early observations yielded only those J^{PC} quantum numbers consistent with a fermion-antifermion bound state. The J^{PC} quantum numbers of a $q\bar{q}$ system with a total quark spin \vec{S} and relative angular momentum \vec{L} are determined as follows: $\vec{J}=\vec{L}+\vec{S}$, $P=(-1)^{L+1}$ and $C=(-1)^{L+S}$. Thus J^{PC} quantum numbers such as 0^{--} , 0^{+-} , 1^{-+} and 2^{+-} are not allowed and are called *exotic* in this context.

Our understanding of how quarks form mesons has evolved within quantum chromodynamics (QCD) and we now expect a richer spectrum of mesons that takes into account not only the quark degrees of freedom but also the gluonic degrees of freedom. Gluonic mesons with no quarks (*glueballs*) are expected. These are bound states of gluons

and since the quantum numbers of low-lying glueballs are not necessarily exotic, they should manifest themselves as extraneous states that cannot be accommodated within $\bar{q}q$ nonets. Indeed there is evidence for a glueball state [1] based on overpopulation of the scalar nonet but identification is complicated since the observed states can be a mixture of a glueball and $\bar{q}q$. Excitations of the gluonic field binding the quarks can also give rise to so-called *hybrid* mesons that can be viewed as bound states of a quark, antiquark and valence gluon ($q\bar{q}g$). An alternative picture of hybrid mesons, one supported by lattice QCD, is one in which a gluonic flux tube forms between the quark and antiquark and the excitations of this flux tube lead to so-called *hybrid* mesons [2]. Conventional $\bar{q}q$ mesons arise when the flux tube is in its ground state. Some hybrid mesons can have a unique signature, exotic J^{PC} , and therefore the spectroscopy of exotic hybrid mesons is not complicated by possible mixing with conventional $\bar{q}q$ states. According to the flux-tube model [2] and lattice gauge calculations [3], one expects the lightest $J^{PC}=1^{-+}$ exotic hybrid to have a mass of about 1.9 GeV/c². In contrast, calculations based on the MIT bag model [4–6] place the mass of the lightest $J^{PC}=1^{-+}$ hybrid meson at about 1.4 GeV/c².

The spectroscopy of exotic mesons provides an attractive

starting point for the study of gluonic excitations. Since flux tubes are thought to be responsible for the confinement mechanism in QCD, experimental information on this spectroscopy is of fundamental importance.

A. Experimental situation

After about two decades of experimental searches there have been reports of experimental observations of states with $J^{PC}=1^{-+}$ by the Brookhaven E852 Collaboration in π^-p interactions at 18 GeV/ c . One of these has a mass of $(1593 \pm 8_{-47}^{+29})$ MeV/ c^2 and width of $(168 \pm 20_{-12}^{+150})$ MeV/ c^2 and decays into $\rho^0\pi^-$ [7,8] and another has a similar mass $(1597 \pm 10_{-10}^{+45})$ MeV/ c^2 , but a larger width $(340 \pm 40_{-50}^{+50})$ MeV/ c^2 , and decays into $\eta'\pi^-$ [9]. The E852 Collaboration also reported observation of another $J^{PC}=1^{-+}$ state with mass $(1370 \pm 16_{-30}^{+50})$ MeV/ c^2 and a width of $(385 \pm 40_{-105}^{+65})$ MeV/ c^2 decaying into $\eta\pi^-$ [10,11]. If an $\eta\pi$ system is in a P wave, the resulting J^{PC} quantum number combination is exotic (1^{-+}). Critical to the identification of this state is not only showing the presence of a P wave, but also that the resulting line shape is consistent with a Breit-Wigner and that the phase motion of the P , as determined by its interference with the dominant D wave cannot be due solely to the $a_2^-(1320)$ resonance. Soon after the E852 report, the Crystal Barrel Collaboration reported an exotic $J^{PC}=1^{-+}$ state produced in $\bar{p}n \rightarrow \pi^-\pi^0\eta$ obtained by stopping antiprotons in liquid deuterium [12]. They reported a mass of $(1400 \pm 20_{-20}^{+20})$ MeV/ c^2 and a width of $(310 \pm 50_{-30}^{+50})$ MeV/ c^2 . A later analysis of $\bar{p}p \rightarrow \pi^0\pi^0\eta$ supported this evidence for an exotic state [13].

The first claim of an exotic meson decaying into $\eta\pi^0$ with a mass of 1400 MeV/ c^2 was made by the GAMS Collaboration in the reaction $\pi^-p \rightarrow \eta\pi^0n$ [14] but a later analysis by the group [15] led to ambiguous results. The VES Collaboration also presented evidence for a P -wave contribution in $\eta\pi$ [16] and at KEK a claim was made for an exotic $\eta\pi$ state [17] as well but with a mass and width close to that of the $a_2(1320)$ and leakage from the dominant D wave could not be excluded.

Indeed, in all the observations, the $\eta\pi$ P wave enhancements have cross sections that are substantially smaller than the dominant $a_2(1320)$ so this leakage, usually due to an imperfect understanding of experimental acceptance, is a source of concern. For example, an observed enhancement in the P wave in the $\rho\pi$ system at low mass was reported in references [7,8] as being due to leakage. Apart from these experimental issues, the interpretation of the nature of low-mass $\eta\pi$ P wave amplitude and phase motion should be guided by the principle of parsimony—less exotic interpretations must also be considered.

This work presents a partial wave analysis (PWA) of the $\eta\pi^0$ system produced in π^-p interactions at an incident momentum of 18 GeV/ c using the E852 apparatus. In this analysis both the η and π^0 are detected through their 2 γ decays. The starting point uses data corresponding to the reaction $\pi^-p \rightarrow 4\gamma n$. A subset of these data correspond to $\pi^-p \rightarrow \pi^0\pi^0n$ and the partial wave analysis of the $\pi^0\pi^0$

system has been reported on in an earlier publication [18]. Here we present the PWA of data from $\pi^-p \rightarrow \eta\pi^0n$.

In contrast to the $\eta\pi^-$ system, charge conjugation C is a good quantum number for the neutral $\eta\pi^0$ system. In the E852 experiment the $\eta\pi^-$ and $\eta\pi^0$ systems have different systematics. The latter relies on measurements from an electromagnetic detector alone while the former also requires information from charged particle tracking in the forward direction. Moreover, as will be discussed below, two resonances dominate the $\pi^-p \rightarrow \eta\pi^0n$ reaction; the scalar (S wave) $a_0(980)$ and the tensor (D wave) $a_2(1320)$ providing benchmarks for the PWA. In contrast, only the $a_2(1320)$ is dominant in the $\pi^-p \rightarrow \eta\pi^-p$ reaction.

B. Outline for this paper

This paper is organized as follows. The experimental overview is presented in Sec. II. Event reconstruction and data selection are described in Sec. III. The details of the PWA formalism and results are given in Sec. IV along with the criteria used to select the physical solution from the set of ambiguous solutions. In Sec. V the results of leakage studies are presented. In Sec. VI the distributions in moments (averages of spherical harmonics) are compared with moments calculated from the PWA solutions. Fits to the moment distributions are also presented. In Sec. VII the mass and t dependence of the PWA solutions are presented and discussed. In particular the t distributions for the D waves are described within the context of Regge phenomenology. The conclusions are summarized in Sec. VIII.

II. EXPERIMENTAL OVERVIEW

The E852 apparatus [19] was built around and included the Multi-Particle Spectrometer (MPS) at BNL. The data used for the analysis reported in this paper were collected in 1994 and 1995 using a nearly pure ($>95\%$) beam of negative pions of momentum 18.3 GeV/ c . A 30-cm-long liquid hydrogen target was surrounded by a cylindrical drift chamber [20] and an array of thallium-doped CsI crystals [21] arranged in a barrel, all located inside the MPS dipole magnet. Drift chambers were used to track charged particles downstream of the target. Two proportional wire chambers (PWC's), downstream of the target, were used in requiring specific charged particle multiplicities in the event trigger. A 3000-element lead glass detector (LGD) [22] measured the energies and positions of photons in the forward direction. The dimensions of the LGD matched the downstream aperture of the MPS magnet. Photons missing the LGD were detected by the CsI array or by a lead-scintillator sandwich array (DEA) downstream of the target and arranged around an aperture to allow for the passage of charged particles.

The first level trigger required that the unscattered or elastically scattered beam not enter an arrangement of two small beam-veto scintillation counters located in front of the LGD. The next level of trigger required that there be no signal in the DEA and no charged particles recorded in the cylindrical drift chamber surrounding the target or in the PWC's (an all-neutral trigger). In the 1994 run all layers of the cylindri-

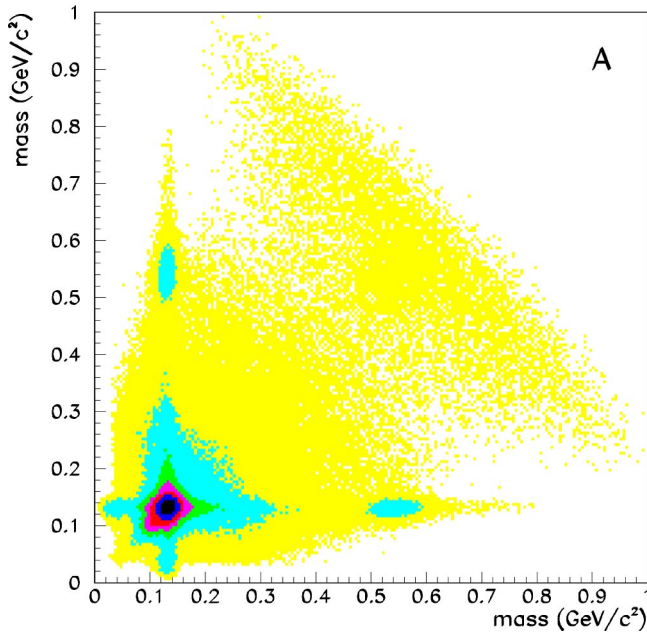


FIG. 1. The plot of pairs of di-photon effective masses (m_{ij} vs m_{kl}) for all pairs of photons (i, j, k, l) is dominated by the $\pi^0\pi^0$ signal. Clear evidence is also seen for the production of $\eta\pi^0$.

cal drift chamber were used in the trigger requirement whereas in the 1995 run, only the outer layer was used. A common off-line analysis criterion required no hits in the cylindrical drift chamber. The final trigger requirement was a minimum deposition of electromagnetic energy in the LGD [22] corresponding to 12 GeV.

The LGD is central to this analysis. The LGD was initially calibrated by moving each module into a monoenergetic electron beam. Further calibration was performed by adjusting the calibration constant for each module until the width of the π^0 and η peaks in the $\gamma\gamma$ effective mass distribution was minimized. The calibration constants were also used for a trigger processor that did a digital calculation of energy deposited in the LGD and the effective mass of photons striking the LGD [22]. A laser-based monitoring system allowed for tracking the gains of individual modules.

Studies were made of various algorithms for finding clusters of energies deposited by photons, including issues of photon-to-photon separation and position finding resolution. These are also described in Ref. [22].

III. EVENT RECONSTRUCTION AND DATA SELECTION

Experiment E852 took data in 1994 and 1995 with an approximate sevenfold increase in statistics collected in 1995 compared to 1994. The combined data sets taken in 1994 and 1995 contain approximately 70 million all-neutral triggered events. Of these events, approximately 13 million were found to have four photons in the LGD. Figure 1 shows a scatterplot of one di-photon effective mass against the other di-photon combination in the event. There are clear indications of the presence of $\pi^0\pi^0$ and $\eta\pi^0$ events in the sample. The single clustering at $m_{\gamma\gamma} = m_{\gamma\gamma} = 0.135 \text{ GeV}/c^2$ is dominated by $\pi^0\pi^0$ events and the two clusterings at $m_{\gamma\gamma}$

$= 0.135 \text{ GeV}/c^2$, $m_{\gamma\gamma} = 0.540 \text{ GeV}/c^2$ are dominated by $\eta\pi^0$ events.

Studies were carried out comparing the 1994 and 1995 data sets for both $\pi^0\pi^0$ and $\eta\pi^0$ events. In each case distributions in the decay angles of the $\pi^0\pi^0$ (or $\eta\pi^0$) system were studied in mass bins of 40 MeV/c^2 and in four bins of t , where t is the square of the momentum transferred from the beam π^- to the outgoing 4γ system. A Kolmogorov test measured the probability that the two distributions (1994 and 1995 data) in each case were consistent with having been drawn from the same parent distribution. The conclusion of this study is that the 1994 and 1995 data sets are statistically indistinguishable.

Events consistent with the production of two π^0 's dominate the sample. The partial wave analysis of the $\pi^0\pi^0$ events is presented in an unpublished thesis of Gunter [23] and in a previous paper [18]. The identification of events from the reaction $\pi^-p \rightarrow \eta\pi^0n$ is described in the unpublished thesis of Lindenbusch [24].

The sample of 45 000 $\pi^-p \rightarrow \eta\pi^0n$ events was selected from the 13 million four photon events by imposing various analysis criteria. It was required that no charged particles were registered in the MPS drift chambers or the cylindrical drift chamber surrounding the liquid hydrogen target. This cut was performed at the pre-reconstruction level and was based on total hit multiplicity. Any event with a photon within 8 cm of the center of the beam hole or the outer edge of the LGD was removed.

Monte Carlo studies were carried out to determine the χ^2 criteria needed to select $\eta\pi^0$ events and eliminate backgrounds from other processes, especially from $\pi^0\pi^0$ events. Events corresponding to $\pi^0\pi^0$, $\eta\pi^0$, $\eta\eta$, and $\eta'\pi^0$ were generated and passed through detector simulation, reconstruction, kinematic fitting, and other event selection software. The χ^2 returned from kinematic fitting to the $\pi p \rightarrow \eta\pi^0n$ reaction hypothesis was required to be less than 7.8 (95% C.L. for a three-constraint fit). The two-constraint χ^2 for the $\pi^0\pi^0$ hypothesis (no requirement that the missing mass be consistent with the neutron mass) was required to be greater than 100. It was found that this latter cut eliminated true $\pi^0\pi^0$ events that have a poor fit to the $\pi p \rightarrow \pi^0\pi^0n$ hypothesis. A further demand was that none of the other final state hypotheses considered ($\eta\eta n$, $\eta'\pi^0n$) had a better χ^2 than that used to select the $\eta\pi^0n$ hypothesis.

The final criterion was that the CsI detector registered less than 20 MeV, a cut which eliminated events with low-energy π^0 's. Background studies [24] estimated the non- η background in the $\pi p \rightarrow \eta\pi^0n$. The signal-to-noise ratio varies from about 5.1:1 in the $\eta\pi^0$ mass region 1.2 to 1.5 GeV/c^2 to 2.5:1 in the $\eta\pi^0$ mass regions below this range and above this range up to 1.8 GeV/c^2 .

The $\eta\pi^0$ effective mass distribution is shown in Fig. 2(a). The $a_0(980)$ and $a_2(1320)$ states, one a scalar and the other a tensor, are clearly observed. The presence of both states is important for this analysis since it provides a basis, as will be discussed below, for selecting the physical solutions from among mathematically ambiguous solutions in doing the partial wave analysis. This distribution in $\eta\pi^0$ effective mass is

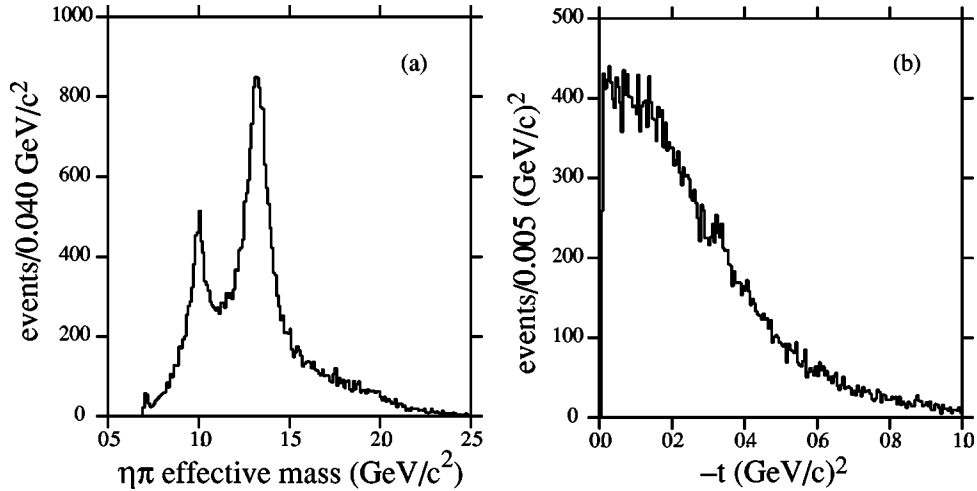


FIG. 2. Distribution in the (a) $\eta\pi^0$ effective mass, (b) momentum-transfer-squared ($-t_{\pi^-\rightarrow\eta\pi}$) from the incoming π^- to the outgoing $\eta\pi^0$ system. These distributions are not corrected for losses due to acceptance.

not corrected for the acceptance of the apparatus but the PWA procedure does take into account the effects of experimental acceptance.

The distribution in $t_{\pi^-\rightarrow\eta\pi}$ is shown in Fig. 2(b). Figure 3 shows the four-photon effective mass distribution for events with a diphoton mass combination consistent with a π^0 and the other di-photon mass either below or above the η mass region for a portion of the total four-photon sample. The resulting $\gamma\gamma\pi^0$ spectra do not show the enhancements at the $a_0(980)$ and $a_2(1320)$ observed in the $\eta\pi^0$ spectrum.

A possible source of background in the $\eta\pi^0$ in the $a_0(980)$ mass region are events corresponding to production

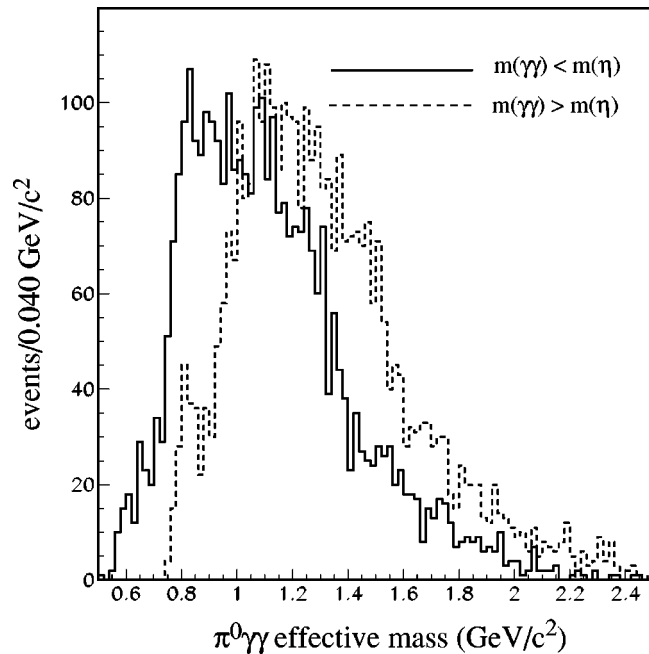


FIG. 3. Distribution in the four photon effective mass for events with a reconstructed π^0 and the other $\gamma\gamma$ effective mass combination falling below (solid) and above (dashed) the η mass region. Neither distribution shows the structure observed for $\eta\pi^0$ events.

of the final state $\eta\pi^0\pi^0n$ and in particular that subset corresponding to $f_1(1285)n$ where the f_1 decays to $a_0\pi^0$. There events can enter the sample under study if one of the π^0 's escapes detection. From a Monte Carlo study of this sample [24] based on a measurement of $f_1(1285)$ production in this experiment [19] it is estimated that at most 10% of the events in the $a_0(980)$ region are due to this background process.

The acceptance in $\eta\pi^0$ effective mass and $t_{\pi^-\rightarrow\eta\pi}$ was estimated by generating Monte Carlo events corresponding to the reaction $\pi^-p\rightarrow\eta\pi^0n$. The acceptance functions as a function of $\eta\pi^0$ effective mass are shown in Fig. 4. The acceptance in $t_{\pi^-\rightarrow\eta\pi}$ increases for $-t$ near zero. This comes about because of the all-neutral requirement in the trigger. The recoil neutron produced in the reaction can interact and cause a signal in the CsI detector thereby vetoing true $\pi^0\pi^0n$ events but for small values of $|t|$ the neutron cannot escape the LH₂ target and the event will not be vetoed.

IV. PARTIAL WAVE ANALYSIS

Partial wave analysis is used to extract production amplitudes (partial waves) from the observed decay angular distributions of the $\eta\pi^0$ system. A process such as $\pi^-p\rightarrow\eta\pi^0n$, dominated by t -channel meson exchange, is conveniently analyzed in the Gottfried-Jackson reference frame. The Gottfried-Jackson frame is defined as a right-handed coordinate system in the center of mass of the produced $\eta\pi^0$ system with the z axis defined by the beam particle momentum and the y axis perpendicular to the plane defined by the beam and recoil neutron momenta. The decay angles (θ, ϕ) are determined by the η four-momentum vector. At a fixed beam momentum, an event is fully specified by $(m_{\eta\pi}, t, \theta, \phi)$. The acceptances of the E852 apparatus for the Gottfried-Jackson angles were studied using Monte Carlo simulations. Results for the $\eta\pi^0$ effective mass region from 1.3 GeV/c^2 to 1.4 GeV/c^2 are shown in Fig. 5.

The production amplitudes and their relative phases are extracted from the accumulated angular distributions, for

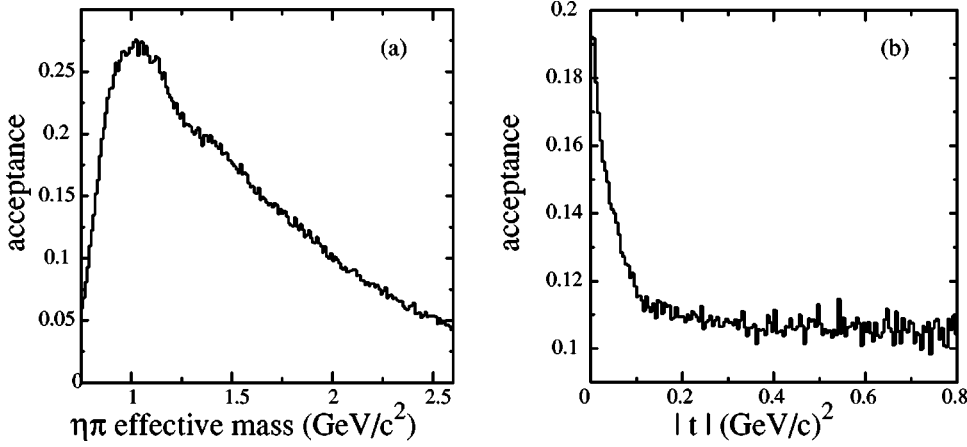


FIG. 4. Acceptance as a function of (a) $\eta\pi^0$ effective mass, (b) momentum-transfer squared ($-t_{\pi^- \rightarrow \eta\pi}$) from the incoming π^- to the outgoing $\eta\pi^0$ system.

bins in $m_{\eta\pi}$ and t , using an extended maximum likelihood fit to the distributions in (θ, ϕ) [23–25]. Fits were performed for three bins in $t_{\pi^- \rightarrow \eta\pi}$ (or simply t) which we label as low- $|t|$ for $|t| < 0.14$ (GeV/c^2), medium- $|t|$ for $0.14 < |t| < 0.31$ (GeV/c^2), and high- $|t|$ for $|t| > 0.31$ (GeV/c^2). For each t bin the PWA fits were performed in 0.04 GeV/c^2 -wide $\eta\pi^0$ mass bins.

Events corresponding to the reaction $\pi^- p \rightarrow \eta\pi^0 n$ were processed through PWA software that extracts partial wave amplitudes and phase differences between various partial waves. This procedure takes into account information about the acceptance of the apparatus. The PWA formalism used in this analysis is model independent since the three-body final state follows from a quasi-two-body interaction. This is in contrast to the *isobar* model needed for more complex final states, for example, in which one makes specific assumptions about a series of sequential decays leading to the final state under consideration.

The decay angular distributions are described by an expansion in partial waves that are products of a production amplitude for a state of angular momentum L and associated magnetic quantum number M and a decay amplitude, also for a given L and M . The angular momentum L is between the η and the π^0 . The production amplitude takes into account the spin degrees of freedom of the initial and final nucleons and the naturality of the exchange particle. That is, the assump-

tion is made that in this peripheral process the produced $\eta\pi^0$ state results from a t -channel exchange from the nucleon vertex to the meson production vertex. Alternatively one can view the production vertex as a time-reversed decay of the produced $\eta\pi^0$ state into the beam particle (π^-) and the exchanged particle.

Parity conservation in the strong interactions implies a relationship between the magnetic quantum number M and naturality. Following Ref. [25] we choose a basis characterized by the naturality of the exchanged particle. *Natural* parity exchange obtains if parity and spin are related as $P = (-1)^J$ (e.g., ρ meson exchange) and the exchange is *unnatural* if $P = (-1)^{J+1}$ (e.g., π meson exchange).

This basis, the *reflectivity* basis, is one that does not possess the mixed symmetries of the D functions or spherical harmonics under rotations about the y axis. For $M > 0$ the linear combination with positive reflectivity, corresponding to natural parity exchange, is

$${}^+D_{M0}^L(\phi, \theta, 0) \equiv \frac{1}{\sqrt{2}} [D_{M0}^L(\phi, \theta, 0) - (-1)^M D_{-M0}^L(\phi, \theta, 0)] \quad (1)$$

and the linear combination with negative reflectivity, corresponding to unnatural parity exchange, is

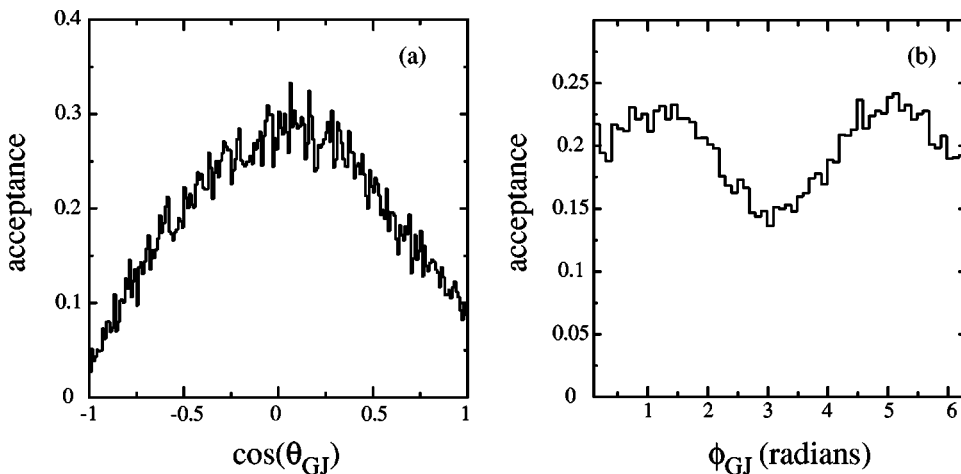


FIG. 5. Acceptance in Gottfried-Jackson angles for the $\eta\pi^0$ effective mass region from 1.3 to 1.4 GeV/c^2 for (a) $\cos(\theta_{\text{GJ}})$, (b) ϕ_{GJ} .

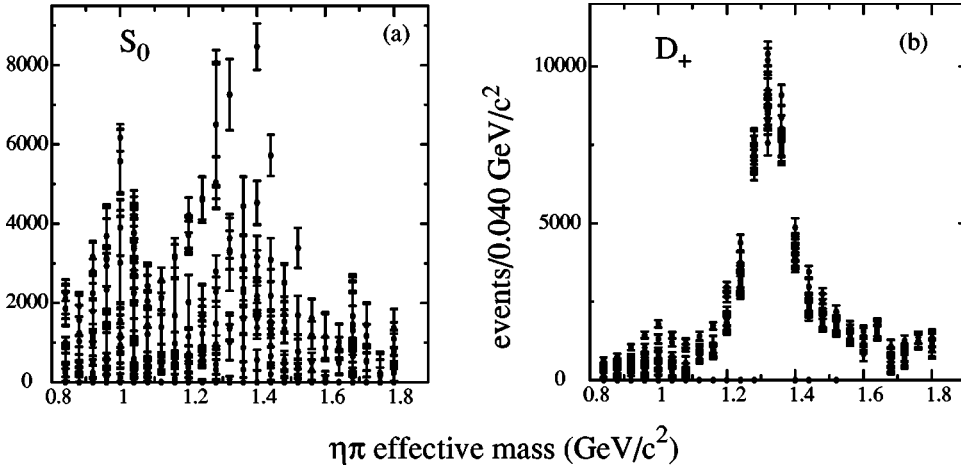


FIG. 6. PWA solution for the (a) S_0 and (b) D_+ waves as a function of $\eta\pi^0$ effective mass. All mathematically ambiguous solutions are shown.

$${}^{-}D_{M0}^L(\phi, \theta, 0) \equiv \frac{1}{\sqrt{2}} [D_{M0}^L(\phi, \theta, 0) + (-1)^M D_{-M0}^L(\phi, \theta, 0)]. \quad (2)$$

For $M=0$ the reflectivity is negative and

$${}^{-}D_{00}^L(\phi, \theta, 0) \equiv D_{00}^L(\phi, \theta, 0). \quad (3)$$

The distribution of events in $m_{\eta\pi}$, t , θ and ϕ is given by

$$I(m_{\eta\pi}, t, \theta, \phi) = \left| \sum_{LM} A_{LM}^+(m_{\eta\pi}, t) {}^{+}D_{M0}^L(\theta, \phi, 0) \right|^2 + \left| \sum_{LM} A_{LM}^-(m_{\eta\pi}, t) {}^{-}D_{M0}^{L*}(\theta, \phi, 0) \right|^2, \quad (4)$$

where the A_{LM} are the production amplitudes and we refer to the various waves as $S_0 \equiv A_{00}^-$, $P_+ \equiv A_{11}^+$, $P_- \equiv A_{11}^-$, $P_0 \equiv A_{10}^-$, $D_+ \equiv A_{21}^+$, $D_- \equiv A_{21}^-$, and $D_0 \equiv A_{20}^-$.

In this analysis we considered $L=0,1,2$ (the nomenclature is S , P , and D , respectively). Waves are further characterized by a subscript 0 if $M=0$ and $+$ or $-$ if $|M|=1$. As noted in Ref. [25], amplitudes with $|M|>1$ are not expected to be important for the production of mesons in πp quasi-two-body processes. This assumption is borne out by PWA fits to these data indicating little contribution from $|M|>1$. We present these results after the discussion of fitting the moments distributions. The amplitudes considered in this analysis, S_0 , P_0 , P_- , D_0 , and D_- are produced via *unnatural* exchange and P_+ and D_+ are produced via *natural* exchange. Waves of different naturality do not interfere. Since the nucleon polarization is not being measured, in Eq. (4) the dependence on the nucleon helicity is implicit in the production amplitude, e.g., $|D_+|^2 = |D_+^{++}|^2 + |D_+^{+-}|^2$ with the upper labels referring to the target and recoil nucleon helicities and the two amplitudes representing nucleon helicity flip and nonflip.

Ambiguities and finding the physical solution. There are multiple discrete sets of partial wave amplitudes that can give rise to exactly the same angular distribution [25]. It can be shown that for the production of two pseudoscalars with

only S , P , and D waves there are up to eight ambiguous solutions. For a given bin in $m_{\eta\pi^0}$ these multiple solutions can be found by randomly seeding the fit (using sets of different initial values for the amplitudes) and doing multiple fits.

It is also possible to find the ambiguous solutions analytically, starting with one of the solutions found from the fitting procedure using the method of Barrelet zeroes [26]. In this analysis the ambiguous solutions found from multiple randomly seeded fits were found to be consistent with the ambiguous solutions found analytically.

As an example, all ambiguous solutions are shown for the S_0 and D_+ waves for the full range in t in Fig. 6. The presence of the dominant $a_2(1320)$ in the D wave leads to a clustering of solutions about the expected Breit-Wigner line shape. The solutions for the S wave are more widely distributed.

When possible, mass-bin to mass-bin continuity along with other independent criteria must be used to select the physical solutions among the ambiguous solutions. In this analysis the presence of the well-established $a_0(980)$ and $a_2(1320)$ states, as observed in the $\eta\pi$ mass distribution, provides a means by which to select the physical solution. For each $m_{\eta\pi}$ mass bin the solution selected as *physical* is one where the S_0 and D_+ amplitudes and the phase difference $\Delta\Phi(D_0 - S_0)$ all as a function of $\eta\pi$ mass, are simultaneously most consistent with two interfering Breit-Wigner amplitudes with masses and widths for the $a_0(980)$ and $a_2(1320)$ as listed by the Particle Data Group (PDG) [27]. For example, referring to Fig. 6, the S_0 amplitude of the physical solution in the 1.0 GeV/c^2 region should be large and its corresponding D_+ amplitude small and in the 1.3 GeV/c^2 mass region the D_+ amplitude should be large and the S_0 amplitude should be small. It was found that the requirement that the S_0 and D_+ solutions simultaneously lie close to the expected line shapes leaves a few ambiguities that are removed when the criterion of proximity to the expected value of $\Delta\Phi(D_0 - S_0)$ is imposed. We note that although the $a_2(1320)$ is dominant in the D_+ wave, the criterion for selection involved the phase difference between the D_0 and S_0 waves—the D_+ and S_0 waves do not interfere. In summary, these criteria were sufficient to uniquely select the physical solution.

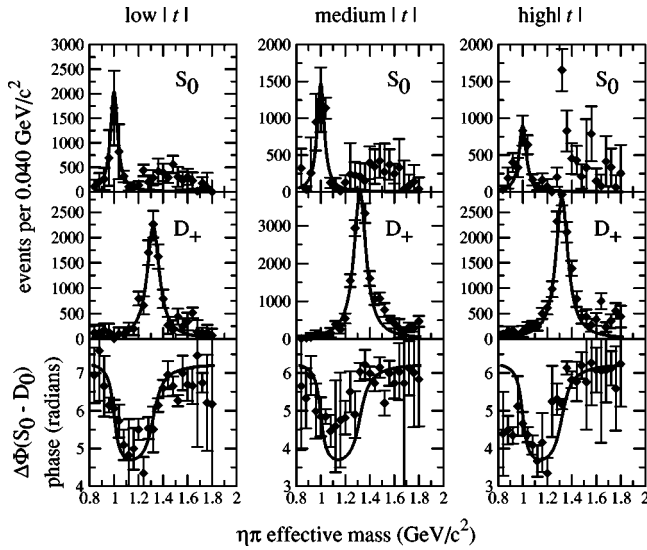


FIG. 7. Physical PWA solution for the (top) S_0 (middle) D_+ waves and (bottom) $\Delta\Phi(S_0 - D_0)$ phase difference for low- $|t|$, medium- $|t|$, and high- $|t|$ as a function of $\eta\pi^0$ effective mass. The curves are the Breit-Wigner line shapes used as criteria for selecting the physical solution and more details are given in the text.

In the discussion below that follows the description of fits to experimentally observed moments distributions, we discuss additional quantitative measures for discarding other ambiguous solutions as well as the effect of their inclusion on the stability of the final results. In addition, as discussed below, the t dependences of the selected D -wave solutions are well-described by Regge phenomenology as is the ratio $(D_0 - D_-)/D_+$, giving us confidence in the selection procedure.

In Fig. 7 the selected physical solution in each of the low- $|t|$, medium- $|t|$, and high- $|t|$ regions is shown as a function of $\eta\pi^0$ mass for the S_0 -wave, D_+ -wave, and the $\Delta\Phi(S_0 - D_0)$ phase difference. Also shown are the corresponding line shapes and phase differences assuming two interfering Breit-Wigner forms for the $a_0(980)$ and $a_2(1320)$ —the basis for the criteria used to select the physical solutions. We note

that the intensity and phase motion of the S_0 wave is also consistent with the presence of both the $a_0(980)$ and the $a_0(1450)$. The $a_0(1450)$ resonance parameters have been extracted from a coupled channel analysis of final states produced in $\bar{p}p$ annihilations [28]. This may account for the excess of events in the 1.4 GeV/c^2 mass region for the S_0 -wave intensity. However, because of the large statistical errors in this region we have not been able to unambiguously extract the $a_0(1450)$ resonance parameters. We will return to this issue in Secs. VI and VII.

V. LEAKAGE STUDIES

Incomplete or incorrect understanding of the experimental acceptance can lead to serious systematic effects in this type of analysis. In particular, it is possible that part of a large, dominant partial wave (for example D_+) could appear as a spurious signal in a different partial wave. We refer to this phenomenon as *leakage* and study it by intentionally using an incorrect model of the acceptance.

A Monte Carlo sample of pure $a_2(1320)$ events was generated including both D_0 and D_+ waves. This Monte Carlo sample included the effects of experimental acceptance. This sample was analyzed in two ways, in one case our best estimate of the acceptance was used, in the second no correction for the acceptance was made.

The analysis using the acceptance correction should produce as output only D_0 and D_+ waves with all others consistent with zero. This was found to be the case and the resulting S_0 and P_+ solutions are compared to the D_+ intensity in Fig. 8(a). A similar result was obtained for all other waves. We conclude that there are no pathological defects in our method since we were able to reproduce correct output from known input.

The second analysis provides an upper limit as to the contribution of leakage in this analysis. The acceptance is known to be significantly different than 100% and a function of the kinematic variables, see, for example, Fig. 4. Approximating the acceptance as equal to 100% independent of the kinematic variables simulates a situation where our under-

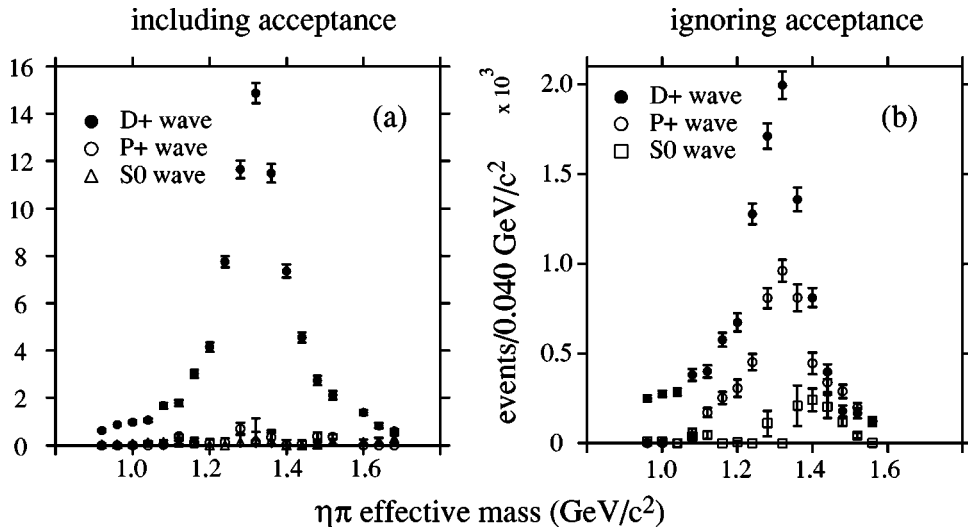


FIG. 8. Results of leakage studies. A sample of Monte Carlo events was generated corresponding to production of the $a_2(1320)$ populating D waves. The sample was passed through cuts simulating detector acceptance and then through the PWA fitting software. In one case (a) the detector acceptance was used in the fitting and in the other (b) the acceptance information was ignored.

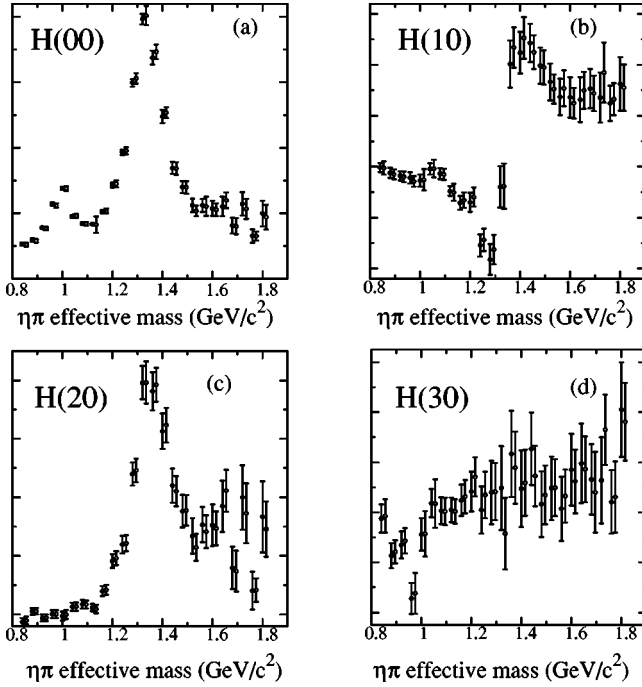


FIG. 9. Comparison between experimentally observed moment distributions (filled circles) and moments calculated using PWA solutions (open circles) as a function of $\eta\pi^0$ effective mass for the moments (a) $H(00)$, (b) $H(10)$, (c) $H(20)$, and (d) $H(30)$. The relation between moments and PWA amplitudes and phase differences is given in the text.

standing of the acceptance is as incorrect as possible, thus providing a limit on the effect of leakage.

It was found that ignoring the acceptance does generate spurious signals in other partial waves. Results for the P_+ and S_0 partial waves are shown in Fig. 8(b). Crucial to the interpretation of this spurious P_+ partial wave is the fact that even when ignoring corrections for the acceptance, the $\Delta\Phi(P_+ - D_+)$ phase difference is independent of mass. As we will show below, the observed $\Delta\Phi(P_+ - D_+)$ phase difference is a strong function of $\eta\pi^0$ mass.

VI. EXPERIMENTAL MOMENTS

To check the results of PWA fitting, moments of the spherical harmonics were calculated for each bin in $m_{\eta\pi^0}$ for each of the three t regions. These moments are labeled as $H(LM)$ and are defined as

$$H(LM) = \int I(\Omega) D_{M0}^{L*}(\phi, \theta, 0) d\Omega. \quad (5)$$

Since

$$H(00) = \int I(\Omega) d\Omega, \quad (6)$$

$H(00)/(4\pi)$ is just the number of events. Moments are directly measured observables and therefore not subject to ambiguities. Given a set of amplitudes, the expected values of the moments can be calculated. If the partial wave expansion

TABLE I. The mass and width for the $a_0(980)$, $a_2(1320)$ and a P -wave resonance obtained from a simultaneous fit to the distributions in each of 12 moments. Details are given in the text. For fit (I) the P -wave mass and width are allowed to float. For fit (II) the P -wave parameters are fixed at the values reported in Ref. [11]. The χ^2 per degree of freedom, χ^2_ν is also given for the two fits.

	low- $ t $	medium- $ t $	high- $ t $
$M_{a_0}(\text{I})$	0.987 ± 0.002	0.980 ± 0.005	1.005 ± 0.01
$M_{a_0}(\text{II})$	0.987 ± 0.002	0.981 ± 0.007	0.990 ± 0.006
$\Gamma_{a_0}(\text{I})$	0.094 ± 0.011	0.246 ± 0.031	0.37 ± 0.050
$\Gamma_{a_0}(\text{II})$	0.094 ± 0.010	0.21 ± 0.04	0.31 ± 0.04
$M_{a_2}(\text{I})$	1.318 ± 0.003	1.329 ± 0.002	1.332 ± 0.003
$M_{a_2}(\text{II})$	1.318 ± 0.003	1.329 ± 0.002	1.335 ± 0.003
$\Gamma_{a_2}(\text{I})$	0.141 ± 0.0093	0.155 ± 0.0067	0.172 ± 0.0092
$\Gamma_{a_2}(\text{II})$	0.141 ± 0.009	0.147 ± 0.007	0.174 ± 0.009
$M_X(\text{I})$	1.386 ± 0.032	9.99 ± 8.77	3.47 ± 0.70
$M_X(\text{II})$	1.37	1.37	1.37
$\Gamma_X(\text{I})$	0.363 ± 0.081	0.11 ± 0.31	0.10 ± 0.27
$\Gamma_X(\text{II})$	0.37	0.37	0.37
$\chi^2_\nu(\text{I})$	1.55	1.40	1.43
$\chi^2_\nu(\text{II})$	1.54	1.70	2.00

is limited to S , P , and D waves with $|M| \leq 1$ there are 12 nonzero moments and the following relations hold:

$$H(00) = |S_0|^2 + |P_0|^2 + |P_-|^2 + |D_0|^2 + |D_-|^2 + |P_+|^2 + |D_+|^2, \quad (7)$$

$$H(10) = \frac{2}{\sqrt{3}} \text{Re}\{S_0 P_0^*\} + \frac{4}{\sqrt{15}} \text{Re}\{P_0 D_0^*\} + \frac{2}{\sqrt{5}} \text{Re}\{P_- D_-^*\} + \frac{2}{\sqrt{5}} \text{Re}\{P_+ D_+^*\}, \quad (8)$$

$$H(11) = \frac{2}{\sqrt{6}} \text{Re}\{S_0 P_-^*\} + \frac{2}{\sqrt{10}} \text{Re}\{P_0 D_-^*\} - \frac{2}{\sqrt{30}} \text{Re}\{P_- D_0^*\}, \quad (9)$$

$$H(20) = \frac{2}{\sqrt{5}} \text{Re}\{S_0 D_0^*\} + \frac{2}{5} |P_0|^2 - \frac{1}{5} |P_-|^2 - \frac{1}{5} |P_+|^2 + \frac{2}{7} |D_0|^2 + \frac{1}{7} |D_-|^2 + \frac{1}{7} |D_+|^2, \quad (10)$$

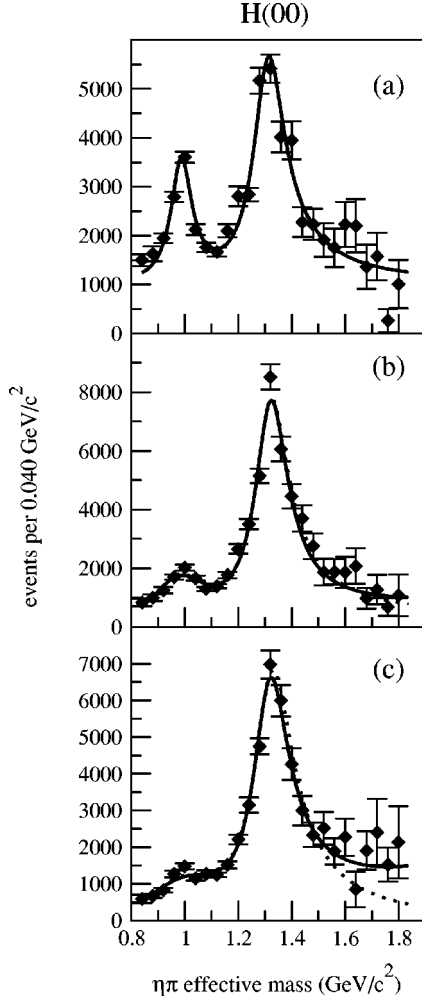


FIG. 10. The observed $H(00)$ moment as a function of $\eta\pi^0$ effective mass for different ranges of momentum-transfer-squared $|t_{\pi^- \rightarrow \eta\pi}|$: (a) low- $|t|$, (b) medium- $|t|$, and (c) high- $|t|$. The curves are results of fits described in the text. $H(00) = |S_0|^2 + |P_0|^2 + |P_-|^2 + |D_0|^2 + |D_-|^2 + |P_+|^2 + |D_+|^2$.

$$H(21) = \frac{2}{\sqrt{10}} \text{Re}\{S_0 D_-^*\} + \frac{2}{5} \sqrt{\frac{3}{2}} \text{Re}\{P_0 P_-^*\} + \frac{2}{7\sqrt{2}} \text{Re}\{D_0 D_-^*\}, \quad (11)$$

$$H(22) = \frac{1}{5} \sqrt{\frac{3}{2}} |P_-|^2 - \frac{1}{5} \sqrt{\frac{3}{2}} |P_+|^2 + \frac{1}{7} \sqrt{\frac{3}{2}} |D_-|^2 - \frac{1}{7} \sqrt{\frac{3}{2}} |D_+|^2, \quad (12)$$

$$H(30) = \frac{6}{7} \sqrt{\frac{3}{5}} \text{Re}\{P_0 D_0^*\} - \frac{6}{7\sqrt{5}} \text{Re}\{P_- D_-^*\} - \frac{6}{7\sqrt{5}} \text{Re}\{P_+ D_+^*\}, \quad (13)$$

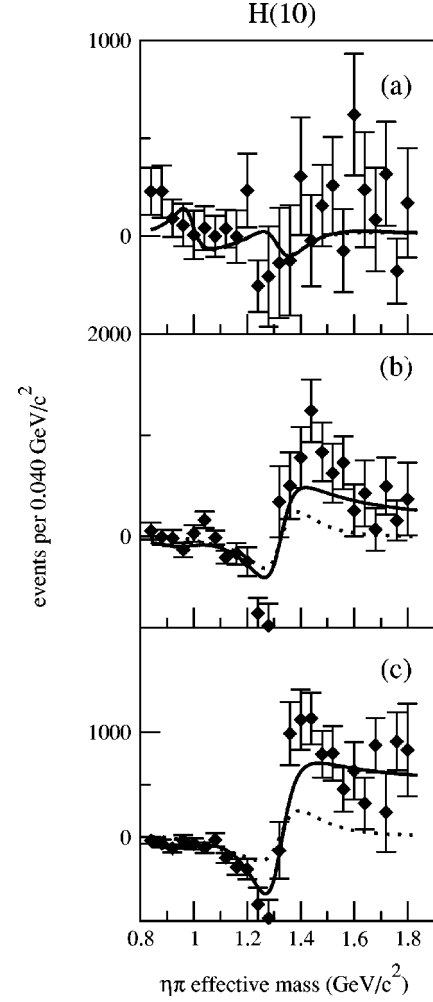


FIG. 11. The observed $H(10)$ moment as a function of $\eta\pi^0$ effective mass for different ranges of momentum-transfer-squared $|t_{\pi^- \rightarrow \eta\pi}|$: (a) low- $|t|$, (b) medium- $|t|$, and (c) high- $|t|$. The curves are results of fits described in the text. $H(10) = 2/\sqrt{3} \text{Re}\{S_0 P_0^*\} + 4/\sqrt{15} \text{Re}\{P_0 D_0^*\} + 2/\sqrt{5} \text{Re}\{P_- D_-^*\} + 2/\sqrt{5} \text{Re}\{P_+ D_+^*\}$.

$$H(31) = \frac{4}{7} \sqrt{\frac{3}{5}} \text{Re}\{P_0 D_-^*\} + \frac{6}{7\sqrt{5}} \text{Re}\{P_- D_0^*\}, \quad (14)$$

$$H(32) = \frac{2}{7} \sqrt{\frac{3}{2}} \text{Re}\{P_- D_-^*\} - \frac{2}{7} \sqrt{\frac{3}{2}} \text{Re}\{P_+ D_+^*\}, \quad (15)$$

$$H(40) = \frac{2}{7} |D_0|^2 - \frac{4}{21} |D_-|^2 - \frac{4}{21} |D_+|^2, \quad (16)$$

$$H(41) = \frac{2}{7} \sqrt{\frac{5}{3}} \text{Re}\{D_0 D_-^*\}, \quad (17)$$

$$H(42) = \sqrt{\frac{10}{21}} |D_-|^2 - \sqrt{\frac{10}{21}} |D_+|^2. \quad (18)$$

We note that the $H(1M)$ and $H(3M)$ moments involve only terms linear in the P wave and the $H(4M)$ moments only involve D waves. The above equations also underscore

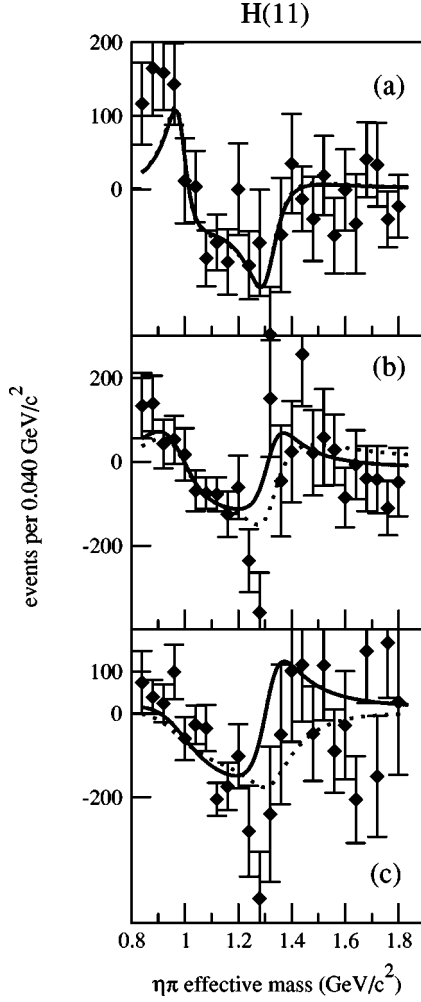


FIG. 12. The observed $H(11)$ moment as a function of $\eta\pi^0$ effective mass for different ranges of momentum-transfer-squared $|t_{\pi^- \rightarrow \eta\pi}|$: (a) low- $|t|$, (b) medium- $|t|$, and (c) high- $|t|$. The curves are results of fits described in the text. $H(11) = 2/\sqrt{6} \operatorname{Re}\{S_0 P_0^*\} + 2/\sqrt{10} \operatorname{Re}\{P_0 D_0^*\} - 2/\sqrt{30} \operatorname{Re}\{P_- D_0^*\}$.

the inherent ambiguities in this partial wave analysis. Solving for the amplitudes and their interferences in terms of the non-ambiguous observable moments does not lead to a unique solution.

In Fig. 9 we show the comparison of moments computed directly from data with those calculated from the above expressions using the selected PWA solutions for the $H(00)$, $H(10)$, $H(20)$, and $H(30)$ moments. The agreement is excellent and similar results were obtained for the other moments.

Fitting the moments. The moments as function of $\eta\pi^0$ mass were fitted using the above equations and assuming Breit-Wigner resonance line shapes for the $a_0(980)$, $a_2(1320)$, and a possible P -wave resonance. These line shapes specify the form of the mass dependence of the amplitudes and phases (interference terms) in the above equations.

A relativistic Breit-Wigner form was used:

$$A_{LM}(m) = \frac{A_{LM} B_L[(qR)^2]}{m^2 - m_r^2 + im_r \Gamma_L(m)}, \quad (19)$$

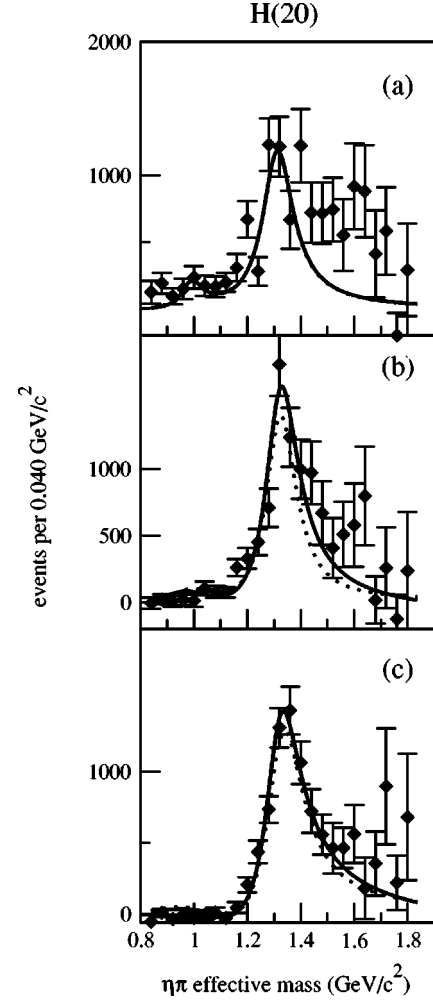


FIG. 13. The observed $H(20)$ moment as a function of $\eta\pi^0$ effective mass for different ranges of momentum-transfer-squared $|t_{\pi^- \rightarrow \eta\pi}|$: (a) low- $|t|$, (b) medium- $|t|$, and (c) high- $|t|$. The curves are results of fits described in the text. $H(20) = 2/\sqrt{5} \operatorname{Re}\{S_0 D_0^*\} + \frac{2}{5}|P_0|^2 - \frac{1}{5}|P_-|^2 - \frac{1}{5}|P_+|^2 + \frac{2}{7}|D_0|^2 + \frac{1}{7}|D_-|^2 + \frac{1}{7}|D_+|^2$.

where $q = \lambda(m, m_\pi, m_\eta)$ is the breakup momentum of mass m . A_{LM} is a complex, mass-independent normalization, and m_r is mass of the resonance. The energy dependent width is given by

$$\Gamma_L(m) = \Gamma_r \left(\frac{q}{q_r} \right) \left(\frac{m_r}{m} \right) \left(\frac{B_L[(qR)^2]}{B_L[(q_r R)^2]} \right)^2 \quad (20)$$

with $q_r = \lambda(m_r, m_\pi, m_\eta)$ and the barrier factors $B_L(x)$ given by $B_0(x) = 1$, $B_1(x) = \sqrt{x/(1+x)}$, $B_2(x) = \sqrt{x^2/[(x-3)^2 + 9x]}$, where the R parametrizes the range of the interaction. In the cross section, phase space introduces a factor of q which multiplies the intensity function given in Eq. (4). Finally the S -wave contribution was modified by adding an incoherent background parametrized as a linear function in $m_{\eta\pi^0}$.

There are 21 parameters allowed to vary in the simultaneous fits to the distributions of the 12 moments as a function of $\eta\pi^0$ mass. The S -, P -, and D -wave Breit-Wigners are

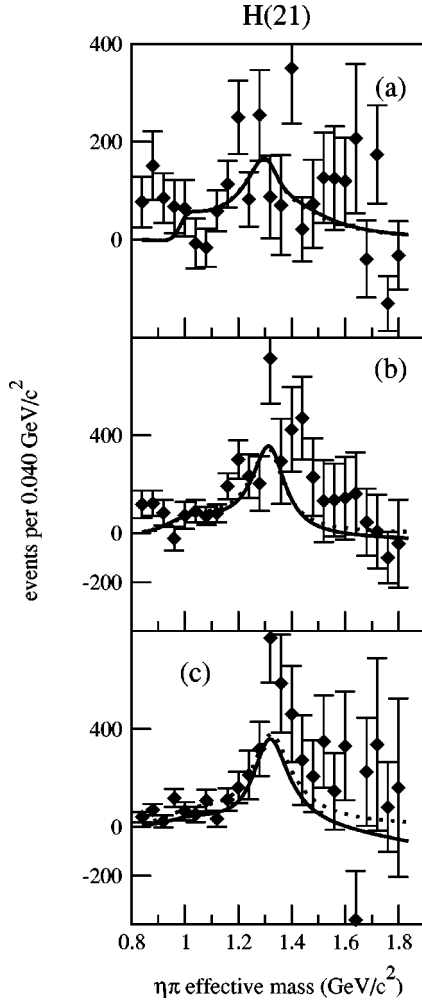


FIG. 14. The observed $H(21)$ moment as a function of $\eta\pi^0$ effective mass for different ranges of momentum-transfer-squared $|t_{\pi^- \rightarrow \eta\pi}|$: (a) low- $|t|$, (b) medium- $|t|$, and (c) high- $|t|$. The curves are results of fits described in the text. $H(21) = 2/\sqrt{10} \text{Re}\{S_0 D_-^*\} + \frac{2}{5}\sqrt{\frac{3}{5}} \text{Re}\{P_0 P_-^*\} + 2/7\sqrt{2} \text{Re}\{D_0 D_-^*\}$.

each characterized by a mass and width for a total of six parameters. Each of the seven waves is characterized by a complex number but the overall phase for each reflectivity is fixed accounting for 12 more parameters. Finally the slope and intercept of the background and the R parameter account for the final three parameters. The values of these parameters resulting from the fits are shown in Table I. We have also attempted to include a second S_0 -wave resonance to account for a possible $a_0(1450)$ in the data. The moment fits were, however, not able to constrain the $a_0(1450)$ resonance parameters. We therefore removed the $a_0(1450)$ from the moments fits. This has no effect on the results and interpretation of the P -wave fits.

The outcome of the fitting is shown for all moments for the three ranges of t described above in Figs. 10–21. The moments shown are corrected for acceptance using the procedure described in Ref. [25]. The solid curves are the result of fits in which all of the 21 parameters described above were allowed to float. The dashed curves are the results of fits where the P -wave Breit-Wigner mass was fixed at

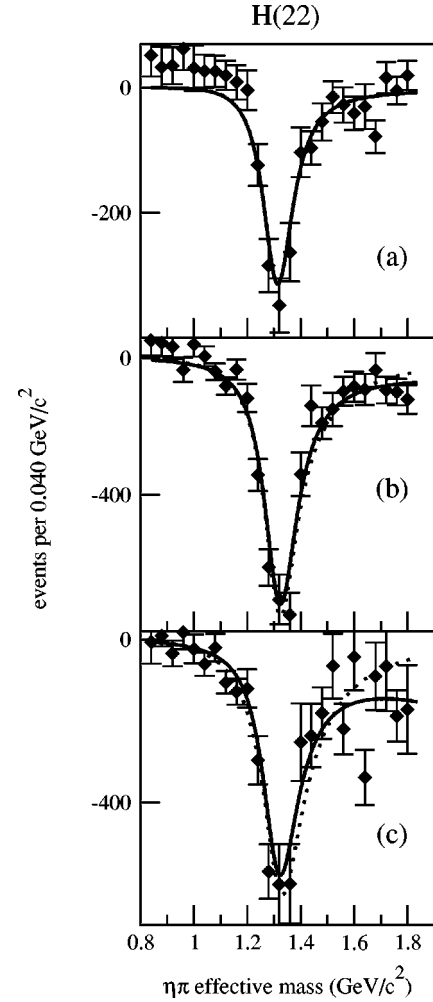


FIG. 15. The observed $H(22)$ moment as a function of $\eta\pi^0$ effective mass for different ranges of momentum-transfer-squared $|t_{\pi^- \rightarrow \eta\pi}|$: (a) low- $|t|$, (b) medium- $|t|$, and (c) high- $|t|$. The curves are results of fits described in the text. $H(22) = \frac{1}{5}\sqrt{\frac{3}{2}}|P_-|^2 - \frac{1}{5}\sqrt{\frac{3}{2}}|P_+|^2 + \frac{1}{7}\sqrt{\frac{3}{2}}|D_-|^2 - \frac{1}{7}\sqrt{\frac{3}{2}}|D_+|^2$.

$1.37 \text{ GeV}/c^2$ and the width was fixed at $0.37 \text{ GeV}/c^2$. These are the parameters reported for the P -wave exotic in the $\eta\pi^-$ channel in Ref. [11].

In the low- t region, the S_0 wave is prominent at $m_{\eta\pi^0} \sim 1 \text{ GeV}/c^2$ and agrees well with the expected contribution to the $\eta\pi^0$ spectrum from the decay of the $a_0(980)$ meson. The S_0 wave is produced without flipping helicities at the meson vertex and therefore it is dominant at low- t and decreases with increasing $|t|$. The structure at $m_{\eta\pi^0} \sim 1 \text{ GeV}/c^2$ in the $H(10)$ and $H(11)$ moments (Figs. 11 and 12, respectively) reflects the interference between the S and P waves and it is noticeable only at low- t where the S -wave production is the strongest. The D_+ wave dominates the spectrum at $m_{\eta\pi^0} \sim 1.3 \text{ GeV}/c^2$ and since it is produced with a meson helicity flip it is suppressed at low- t and it is the largest in the medium- t region. In all three t -regions, however, it is well described by a Breit-Wigner shape corresponding to the $a_2(1320)$ meson. As the D_+ production increases (to medium and large t regions), the structure in the

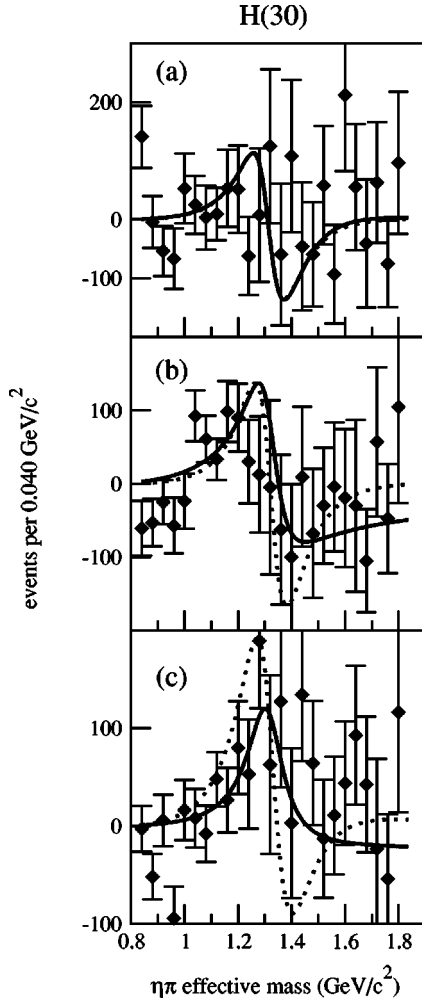


FIG. 16. The observed $H(30)$ moment as a function of $\eta\pi^0$ effective mass for different ranges of momentum-transfer-squared $|t_{\pi^- \rightarrow \eta\pi}|$: (a) low- $|t|$, (b) medium- $|t|$, and (c) high- $|t|$. The curves are results of fits described in the text. $H(30) = \frac{6}{7} \sqrt{\frac{3}{5}} \text{Re}\{P_0 D_0^*\} - 6/7 \sqrt{5} \text{Re}\{P_- D_-^*\} - 6/7 \sqrt{5} \text{Re}\{P_+ D_+^*\}$.

moment $H(10)$ (Fig. 11) moves to the a_2 region and a similar structure in the moment $H(30)$ (Fig. 16) appears. Similarly, the interference of the negative reflectivity P waves with the negative reflectivity D waves is reflected in the moments $H(11)$ and $H(31)$ (Figs. 12 and 17, respectively) at $m_{\eta\pi^0} \sim 1.3 \text{ GeV}/c^2$.

The fit corresponding to the fixed P -wave parameters (dashed curve) is significantly worse in $H(10)$ (Fig. 11)—a moment linear in the P -wave and somewhat worse or no better in the other moments that are linear in the P -wave— $H(11)$ (Fig. 12), $H(30)$ (Fig. 16) and $H(31)$ (Fig. 17). In addition to the $H(00)$ moment distribution, the other moments— $H(20)$, $H(22)$, $H(40)$, and $H(42)$ —are primarily sensitive to the presence of the a_2 meson, and therefore are not very sensitive to treatment of P -waves in the fit. The fit with the P -wave parameters fixed gives a significantly worse χ^2 per degree of freedom (χ_ν^2 from 1.70 to 2.00) as compared to the case when the P -wave parameters are allowed to float (χ_ν^2 from 1.37 to 1.43). In the later case, how-

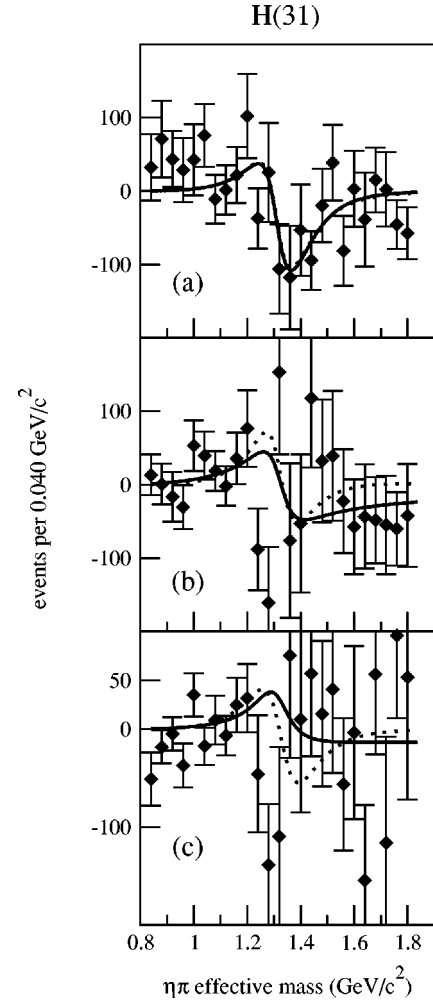


FIG. 17. The observed $H(31)$ moment as a function of $\eta\pi^0$ effective mass for different ranges of momentum-transfer-squared $|t_{\pi^- \rightarrow \eta\pi}|$: (a) low- $|t|$, (b) medium- $|t|$, and (c) high- $|t|$. The curves are results of fits described in the text. $H(31) = \frac{4}{7} \sqrt{\frac{3}{5}} \text{Re}\{P_0 D_0^*\} + 6/7 \sqrt{5} \text{Re}\{P_- D_0^*\}$.

ever, it was found that no single set of consistent parameters could be found for the P waves across the three t ranges. In the low- t range the P wave with mass of $1.39 \text{ GeV}/c^2$ and width of $0.36 \text{ GeV}/c^2$ was found, which is the only solution consistent with what was reported for the $\eta\pi^-$ channel [11]. However, even in this t range other solutions could also be found with masses ranging from 1 to 5 GeV/c^2 . For example, a solution for a P wave with a mass of $0.91 \text{ GeV}/c^2$ and a width of $1.05 \text{ GeV}/c^2$ had a $\chi_\nu^2 = 1.57$. This is because the interference with the D waves is weak at low- t and the S wave is too narrow to constrain the P away from the $m_{\eta\pi^0} \sim 1.3 \text{ GeV}/c^2$ region. The medium- t to large- t range should be the best for constraining the P waves. Here the D waves are dominant and some S wave is still present. In this t range, however, acceptable solutions (with comparable χ_ν^2) different from the one listed in Table I could not be found.

The nonvanishing moments $H(10)$ (Fig. 11), $H(11)$ (Fig. 12), $H(30)$ (Fig. 16), $H(31)$ (Fig. 17), and $H(32)$ (Fig. 18) clearly indicate a presence of a P wave in the $\eta\pi^0$ system.

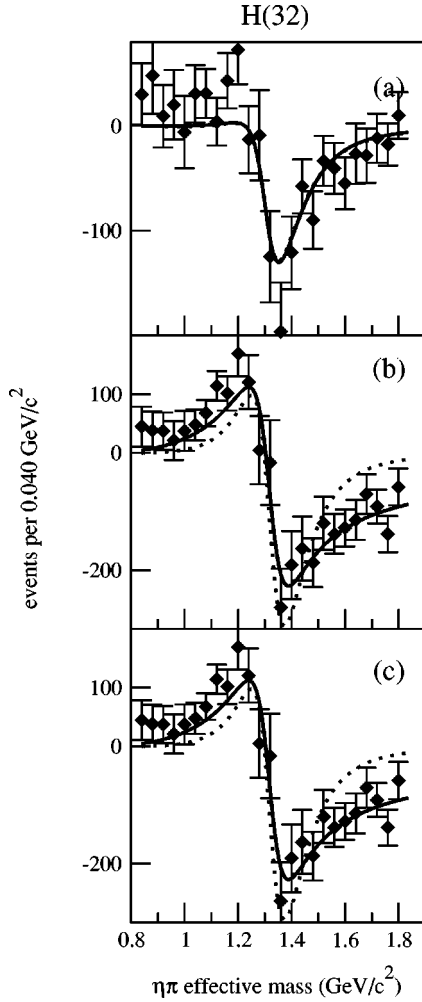


FIG. 18. The observed $H(32)$ moment as a function of $\eta\pi^0$ effective mass for different ranges of momentum-transfer-squared $|t_{\pi \rightarrow \eta\pi}|$: (a) low- $|t|$, (b) medium- $|t|$, and (c) high- $|t|$. The curves are results of fits described in the text. $H(32) = \frac{2}{7} \sqrt{\frac{3}{2}} \text{Re}\{P_- D_-^*\} - \frac{2}{7} \sqrt{\frac{3}{2}} \text{Re}\{P_+ D_+^*\}$.

The large values of mass and width found indicate that the Breit-Wigner parametrization for these waves is most likely inadequate.

VII. MASS AND t DEPENDENCE OF PARTIAL WAVES

A. PWA solutions and fits to the moments

In Figs. 22–24 various partial waves and phase differences are shown as a function of $\eta\pi^0$ mass for the low- $|t|$, medium- $|t|$, and high- $|t|$ ranges. In particular we show the mass dependence of the S_0 and D_0 amplitudes and the $\Delta\Phi(S_0 - D_0)$ phase difference. Also shown is the mass dependence of the P_+ and D_+ amplitudes and the $\Delta\Phi(P_+ - D_+)$ phase difference. The filled data points indicate the selected (physical) solutions. The additional points indicated by open circles and dashed error bars are those ambiguous solutions that satisfy the conditions described below.

The curves are the result of the fits to the moments where the P -wave Breit-Wigner parameters are allowed to float. We

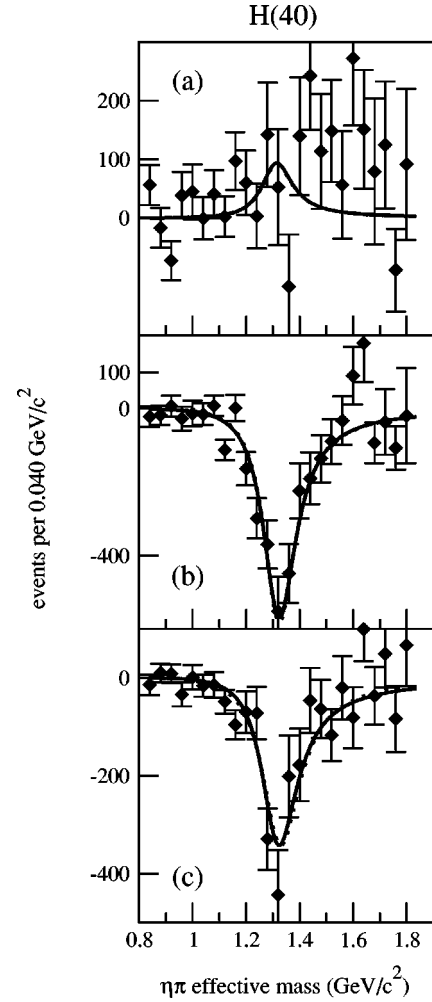


FIG. 19. The observed $H(40)$ moment as a function of $\eta\pi^0$ effective mass for different ranges of momentum-transfer-squared $|t_{\pi \rightarrow \eta\pi}|$: (a) low- $|t|$, (b) medium- $|t|$, and (c) high- $|t|$. The curves are results of fits described in the text. $H(40) = \frac{2}{7} |D_0|^2 - \frac{4}{21} |D_-|^2 - \frac{4}{21} |D_+|^2$.

refer the reader to similar plots shown in Fig. 7 for the S_0 and D_+ amplitudes and the $\Delta\Phi(S_0 - D_0)$ phase difference along the curves used to select the solutions.

The results of the fits to the moments (recalling that the moments are unambiguous) were used to study the possible inclusion of other ambiguous solutions not selected as the physical solutions. We compute a χ^2 that measures the deviation of other ambiguous solutions from the partial wave solutions obtained from the moments fits. This requirement was imposed separately for the S_0 and D_+ waves and the $\Delta\Phi(S_0 - D_0)$ phase difference. In some cases several ambiguous solutions were found to have χ^2 similar to the selected solutions and these are included in Figs. 22–24 as the open circles with dashed error bars. The mass-dependent fits involving only the P_+ and D_+ amplitudes and the $\Delta\Phi(P_+ - D_+)$ —as described below—phase difference were insensitive to the inclusion of these solutions.

The fits shown in Figs. 22–24 describe the D_0 and D_+ in all three $|t|$ regions. The values obtained for the mass and width of the $a_2(1320)$ as shown in Table I are consistent

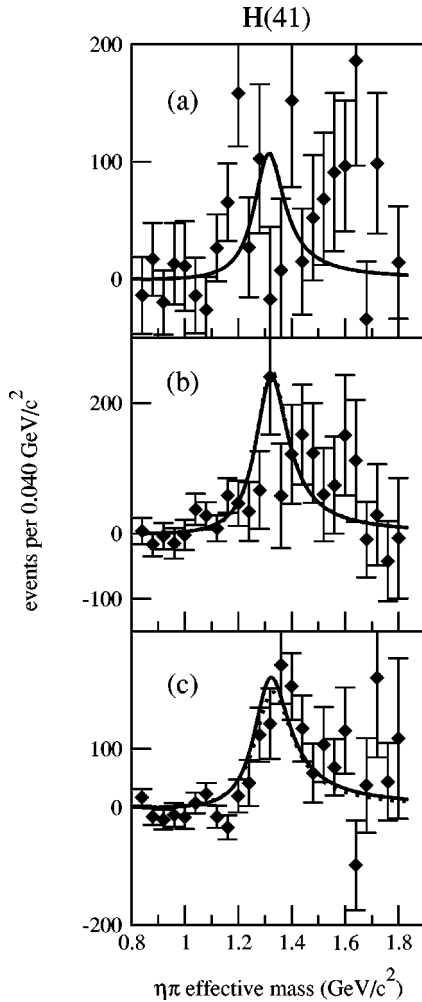


FIG. 20. The observed $H(41)$ moment as a function of $\eta\pi^0$ effective mass for different ranges of momentum-transfer-squared $|t_{\pi \rightarrow \eta\pi}|$: (a) low- $|t|$, (b) medium- $|t|$, and (c) high- $|t|$. The curves are results of fits described in the text. $H(41) = \frac{2}{7} \sqrt{\frac{5}{3}} \text{Re}\{D_0 D_-^*\}$.

with nominal values for this well understood state. The S_0 is well described in the low- $|t|$ region and the mass and width shown in Table I for the $a_0(980)$ agree with published values. As $|t|$ increases the production of the $a_0(980)$ decreases and the description of the S_0 wave in Fig. 24, for the high- $|t|$ range is problematic. In this region the S_0 wave includes mostly structureless background naturally subsumed into the S_0 wave. Requiring that the S_0 wave be described by a Breit-Wigner wave yields a width that is wide and driven by the phase motion of the $a_2(1320)$ via the $\Delta\Phi(S_0 - D_0)$ phase difference. As noted above, the moment fits did not constrain the parameters of a possible second scalar resonance, the $a_0(1450)$. In the mass-dependent amplitude and phase difference fits, the inclusion of a second scalar resonance in the low- t region yields $M = 1.34 \pm 0.06$ GeV and $\Gamma = 0.41 \pm 0.09$ GeV for the mass and width of the second a_0 resonance, while in the medium- t region we obtain $M = 1.44 \pm 0.03$ GeV and $\Gamma = 0.25 \pm 0.06$ GeV, respectively. No stable fit was found for high- t data.

The moments fits poorly describe the P_+ waves in all three $|t|$ regions and the P_+ amplitude peaks in the vicinity

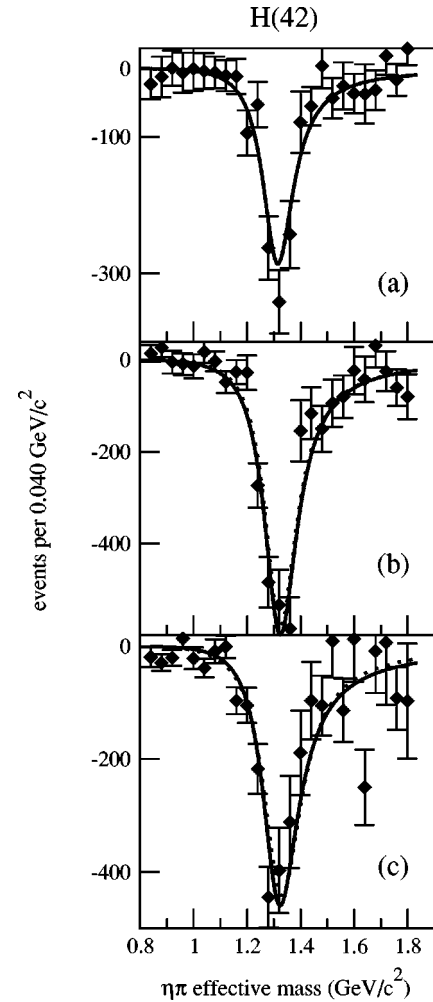


FIG. 21. The observed $H(42)$ moment as a function of $\eta\pi^0$ effective mass for different ranges of momentum-transfer-squared $|t_{\pi \rightarrow \eta\pi}|$: (a) low- $|t|$, (b) medium- $|t|$, and (c) high- $|t|$. The curves are results of fits described in the text. $H(42) = \sqrt{10/21} |D_-|^2 - \sqrt{10/21} |D_+|^2$.

of the dominant D_+ wave strongly suggesting leakage. We also note that the P_+ wave has an additional lower mass peak in the vicinity of the $a_0(980)$ in the low- $|t|$ region [see Figs. 22 and 23 where production of the $a_0(980)$ is strong—again suggesting leakage]. Our Monte Carlo studies indicate that leakage of dominant waves can lead to false peaks in other amplitudes but it is unlikely to cause false phase motion. Indeed this P_+ wave enhancement at about the mass of the $a_0(980)$ follows closely the behavior of the S wave in its dependence on both mass and momentum transfer squared. Furthermore as shown in Fig. 22 and especially in Fig. 23 the additional solutions allowed by the selection criteria (those indicated by open circles) do not alter the S wave shape but reduce the amplitude of the P_+ wave in the region of ~ 1 GeV/ c^2 . Furthermore, the fits to the moments do not reveal any P wave signal at ~ 1 GeV/ c^2 and due to angular momentum barrier effects it is expected that at low breakup momentum the S wave should dominate over the P wave.

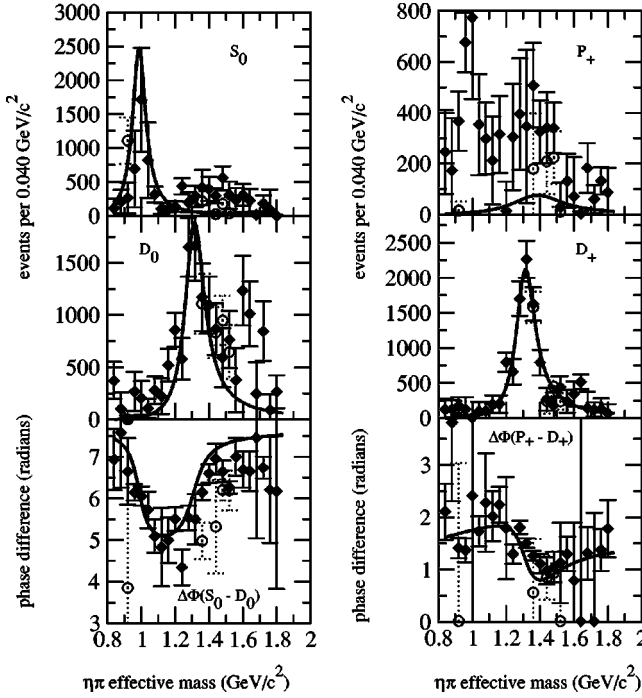


FIG. 22. PWA solutions for the (left top) S_0 and (left middle) D_0 waves and (left bottom) $\Delta\Phi(S_0 - D_0)$ phase difference and for the (right top) P_+ and (right middle) D_+ waves and (right bottom) $\Delta\Phi(P_+ - D_+)$ phase difference for the low- $|t|$ region. The fits are a result of the fit to the moments. The filled diamonds correspond to the selected solution. The open circles are additional solutions allowed by the criteria described in the text.

B. Systematics and the fitting procedure

The assumption was made earlier that waves with $|M| > 1$ were not important. In order to test this assumption the additional $|M|=2$ D waves, one for each reflectivity, were included in the fits for all the moments including the $H(43)$ and $H(44)$ moments. The Breit-Wigner distributions corresponding to the resulting fits are shown in Fig. 25 for the D_+ , D_0 , D_- waves and the two $D_{M=2}$ waves of opposite reflectivities (the two $M=2$ curves are indistinguishable in the plot). This supports our original assumption.

The systematics of varying all possible fit assumptions was studied for the D_+ -wave for the high- $|t|$ region and the results are shown in the plot of Fig. 26. We chose to study this high- $|t|$ region since the description of the D_+ wave amplitude is poorest for this region (see Fig. 24). The curve is the result of the overall fit to the moments. The shaded region corresponds to the variations in the fit by letting the Breit-Wigner parameters for all the other waves vary in all possible combinations—that is, being fixed at nominal values or allowed to float. The D_+ wave is within the systematic errors.

C. Mass-dependent fits

The dependence of the measured D_+ and P_+ amplitudes and the $\Delta\Phi(P_+ - D_+)$ phase difference as a function of $\eta\pi^0$ mass was fitted to two interfering Breit-Wigner line shapes following the method of Ref. [11]. Fits carried out

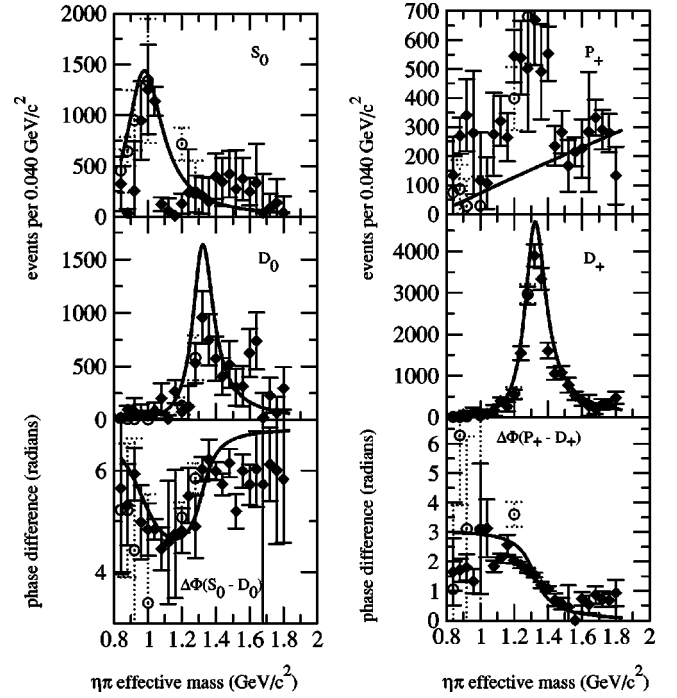


FIG. 23. PWA solutions for the (left top) S_0 and (left middle) D_0 waves and (left bottom) $\Delta\Phi(S_0 - D_0)$ phase difference and for the (right top) P_+ and (right middle) D_+ waves and (right bottom) $\Delta\Phi(P_+ - D_+)$ phase difference for the medium- $|t|$ region. The fits are a result of the fit to the moments. The filled diamonds correspond to the selected solution. The open circles are additional solutions allowed by the criteria described in the text.

separately for the three ranges in t are presented in the plots of Fig. 27 and the fit parameters are listed in Table II. In Fig. 28 the P -wave parameters obtained from the mass dependent fits are compared to those reported in Refs. [11–13]. The P -wave mass obtained for the high- t range is consistent with that reported in the $\eta\pi^-$ channel but the width observed here is significantly higher. The values obtained for the mass in the low- t and high- t ranges are lower than for the $\eta\pi^-$ channel. The conclusion is that no consistent set of resonant P -wave parameters can describe the data while the resonant parameters obtained for the $a_2(1320)$ are consistent for various ranges in $\eta\pi^0$ mass and $|t|$ and consistent with well-established parameters from earlier experiments.

D. Description of the t dependence of the D waves

Figure 29 shows the dependence of the D_+ , D_0 , and D_- waves as a function of $t_{\pi^- \rightarrow \eta\pi}$. Since the $a_2(1320)$ is dominant in these waves and the production of these waves is associated with exchanges well known from Regge phenomenology, a comparison of data with this known phenomenology is a check on the methodology. Indeed the t dependence is well described.

The D_+ wave is produced via a natural t -channel charge exchange which is dominated by the ρ trajectory and is parametrized by [29]

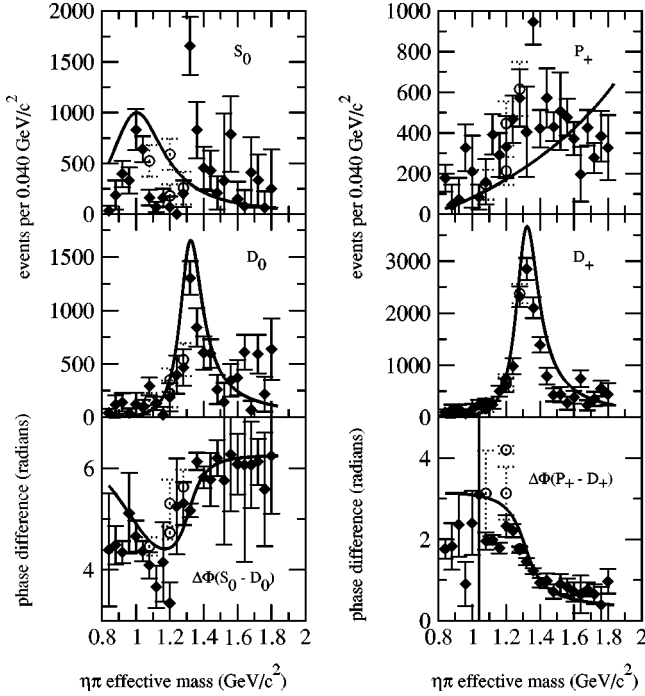


FIG. 24. PWA solutions for the (left top) S_0 and (left middle) D_0 waves and (left bottom) $\Delta\Phi(S_0 - D_0)$ phase difference and for the (right top) P_+ and (right middle) D_+ waves and (right bottom) $\Delta\Phi(P_+ - D_+)$ phase difference for the high- $|t|$ region. The fits are a result of the fit to the moments. The filled diamonds correspond to the selected solution. The open circles are additional solutions allowed by the criteria described in the text.

$$D_+^{++} = i \sqrt{-\frac{t'}{4m_N^2} \left(1 - \frac{t}{m_a^2}\right)^2} e^{b\rho t} e^{-i\pi\alpha_\rho(t)/2} \times \Gamma[1 - \alpha_\rho(t)] \sin[\pi\alpha_\rho(t)/2] \quad (21)$$

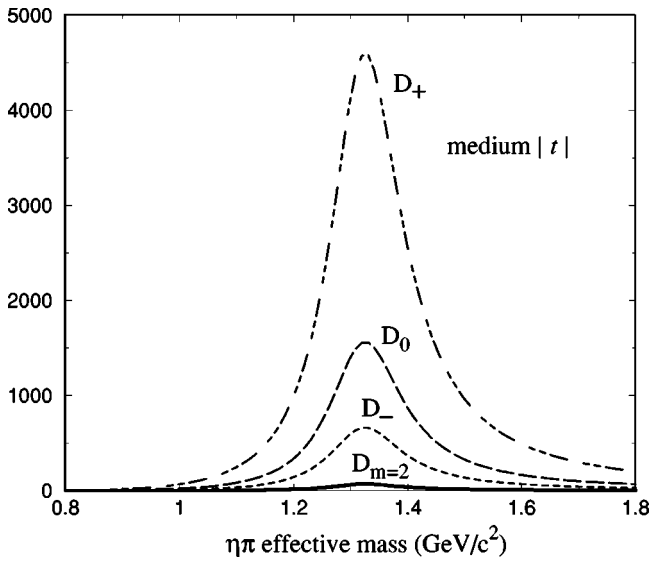


FIG. 25. Comparison of the intensity of the D waves for the medium- $|t|$ region including the D waves with $M=2$. There are two $M=2$ waves with opposite reflectivity.

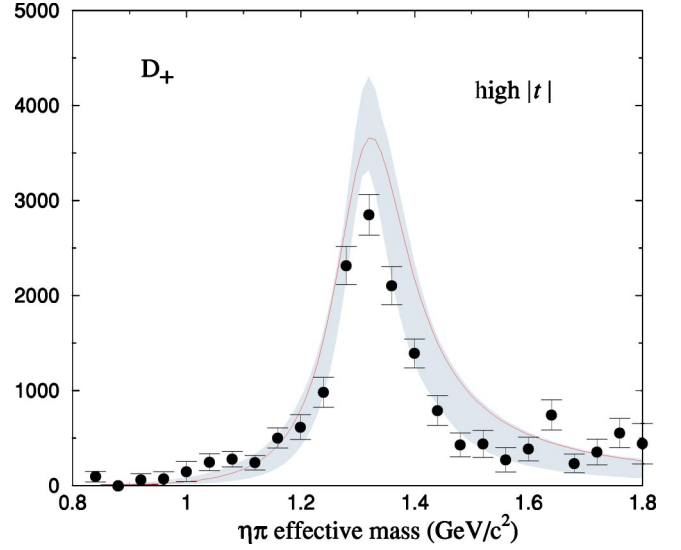


FIG. 26. The D_+ wave as a function of $\eta\pi^0$ effective mass for the high- $|t|$ range. The curve is the result of an overall fit to the moments, including a D -wave resonance, as described in the text. The shaded area is an estimate of the systematic errors derived from a variation of all combinations of the Breit-Wigner parameters for the S , P , and D amplitudes—as described in the text.

$$D_+^{+-} = r \sqrt{\frac{-t'}{4m_N^2}} D_+^{++}. \quad (22)$$

Here the D_+^{+-} and D_+^{++} are the nucleon helicity flip and nonflip amplitudes, respectively, with $r=7$ in Eq. (22) according to Ref. [29] and

$$|D_+|^2 = |D_+^{++}|^2 + |D_+^{+-}|^2. \quad (23)$$

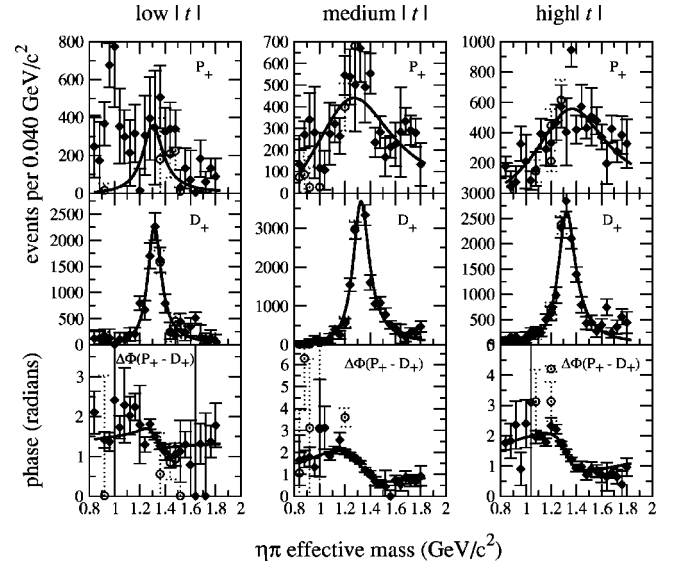


FIG. 27. PWA solution for the (top) P_+ and (middle) D_+ waves and (bottom) $\Delta\Phi(P_+ - D_+)$ phase difference for low- $|t|$, medium- $|t|$, and high- $|t|$ as a function of $\eta\pi^0$ effective mass. The curves are the result of a mass-dependent fit assuming Breit-Wigner resonance forms for the P_+ and D_+ waves.

TABLE II. The masses and widths obtained from a simultaneous fit to D_+ intensity, the P_+ intensity and the $\Delta\Phi(P_+-D_+)$ phase difference. For these fits both waves are parametrized as Breit-Wigner resonances. In addition to the fits for the three ranges of t we also include the fit for the full t range to compare with the results of Ref. [11].

	all $ t $	low- $ t $	medium- $ t $	high- $ t $
M_{a_2}	1.326	1.316	1.329	1.326
	± 0.0023	± 0.0049	± 0.0029	± 0.0036
Γ_{a_2}	0.169	0.127	0.154	0.166
	± 0.0069	± 0.014	± 0.0082	± 0.01
M_X	1.272	1.301	1.268	1.356
	± 0.017	± 0.014	± 0.023	± 0.021
Γ_X	0.66	0.19	0.67	0.629
	± 0.048	± 0.032	± 0.087	± 0.064
χ^2_ν	3.23	2.13	1.51	1.60

The parameters of the ρ trajectory are given by $\alpha_\rho(t) = 0.5 + 0.9t[\text{GeV}^2]$, $b_\rho = 3.25 \text{ GeV}^{-2}$ [30]. The fit of the t -distribution given by Eq. (22) to the measured t distribution involves one parameter—the overall normalization—and is shown in Fig. 29. Some discrepancy is seen at large t , in particular the characteristic dip of the ρ exchange at $t = m_\rho^2$ is not seen. This indicates that there is some absorption required for the a_2 .

The D^0 wave is produced via unnatural exchange and is expected to be dominated by the b_1 in the nucleon helicity flip amplitude and the tensor, Z trajectory ($J^{PC}I = 2^{- - 1}$) in the nonflip amplitude. These can be parametrized by [29]

$$D_0^{+-} = i \sqrt{\frac{-t'}{4m_N^2}} \left(1 - \frac{t}{m_a^2}\right) e^{b_{b_1} t} \times e^{-i\pi\alpha_{b_1}(t)/2} \times \Gamma[-\alpha_{b_1}(t)] \sin[\pi\alpha_{b_1}(t)/2], \quad (24)$$

$$D_0^{++} = e^{b_Z t} e^{-i\pi\alpha_Z(t)/2} \Gamma[1 - \alpha_Z(t)] \cos[\pi\alpha_Z(t)/2] \quad (25)$$

with the parameters of the two trajectories given by $\alpha_{b_1} = -0.37 + 0.9t [\text{GeV}^2]$, $\alpha_Z = 0.9t [\text{GeV}^2]$, and $b_{b_1} = b_Z = b_\pi = 4.51 \text{ GeV}^{-2}$ [30].

The D_- wave is produced by unnatural parity exchange and its t dependence is given by $D_-(t) = \sqrt{-t'/4m_N^2} \dot{D}_0(t)$. The fit to the measured D_0 wave intensity has two parameters—the normalization of the nucleon helicity flip and nonflip amplitudes—and is also shown in Fig. 29.

E. Ratio of D waves

In a paper discussing the PWA of the $\eta\pi$ system produced in peripheral πp interactions [31], Sadovsky uses a criterion for selecting the physical solution among the ambiguous solutions. The test involves a measurement of the ratio $r_S = (D_0 - D_-)/D_+$. According to Regge phenomenology this ratio should fall as α/p_π where α is determined from other experiments. At $p_\pi = 18 \text{ GeV}/c$ this ratio is expected to be $r_S = 0.80$. Integrating the distributions in Fig. 29 over all t we obtain $r_S = 0.72 \pm 0.12$.

VIII. CONCLUSIONS

A partial wave and moment (averages of spherical harmonics) analysis of data collected in experiment E852 from the reaction $\pi^- p \rightarrow \eta\pi^0 n$ (where $\eta \rightarrow \gamma\gamma$) as a function of $\eta\pi^0$ effective mass and momentum-transfer-squared was performed. The presence of two well-established $a_0(980)$ and $a_2(1320)$ resonances allows for the imposition of criteria for selecting the physical solution among the mathematically ambiguous solutions. The physical solution is consistent with the presence of two interfering Breit-Wigner resonances for these states. The distribution in 12 acceptance-corrected moments $H(L, M)$ calculated directly from the data are consistent with moments calculated from the PWA solutions.

Every term in the moments with *odd* L (5 of the 12) is linear in the P wave and the observed moments distributions are nonzero clearing indicating that the data demand the presence of a P wave. To allow for the inclusion of a possible resonance with exotic quantum numbers, the moments are

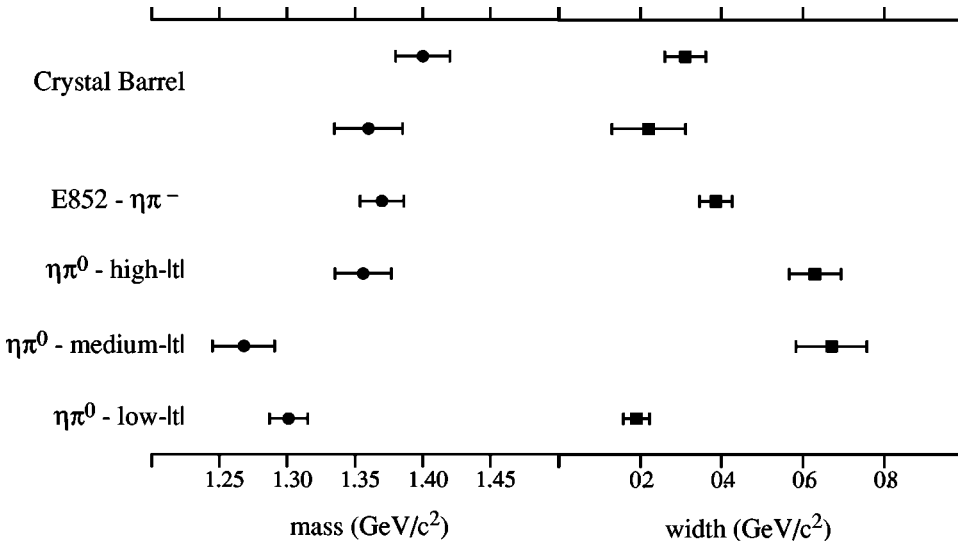


FIG. 28. Comparison of P -wave mass and widths among various studies. A mass dependent fit to the D_+ and P_+ amplitudes and $\Delta\Phi(P_+-D_+)$ phase difference, assuming Breit-Wigner line shapes was carried out for the E852 data for $\eta\pi^0$ (this study) and $\eta\pi^-$. Results are also compared to the Crystal Barrel results.

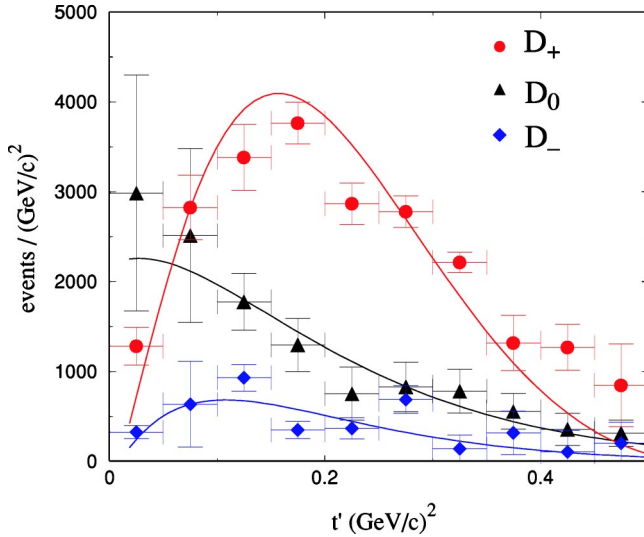


FIG. 29. Dependence of D_+ (circles), D_0 (triangles), and D_- (diamonds) waves on $|t'|$ or $|t_{\pi^- \rightarrow \eta\pi} - t_{\min}|$. The curves are the results of fits to forms for these distributions expected from Regge phenomenology.

thus fit with the assumption of three interfering Breit-Wigner resonances for the S , and D , and P waves.

The data suggest weak production of the $a_0(1450)$. The $a_0(1450)$ was established by the Crystal Barrel Collaboration in $\bar{p}p \rightarrow \pi^0 \pi^0 \eta$ and $\bar{p}p \rightarrow \pi^0 \eta \eta$ [28] with production ratios for $a_0(1450):a_0(980):a_2(1320)$ equal to 4:6:33 and 11:14:25, respectively. These are qualitatively consistent with our results. The dominant D_+ , D_0 , and D_- waves are consistent with production of the $a_2(1320)$ and fits to their line shapes are consistent with the resonance parameters of this well-established tensor resonance. Moreover, the observed t dependence of the individual D waves are well described by Regge phenomenology as is their ratio. Finally the a_0 and a_2 in the data are well described as Breit-Wigner resonances produced via a t -channel exchange mechanisms regardless the treatment of the P wave and/or incoherent background.

While the Breit-Wigner parametrization of the S wave and D wave is physically well motivated and confirmed by the

data, the resonance representation of the P wave is problematic. The data unambiguously indicated that the phase of the P wave increases as the function of the $\eta\pi^0$ mass which corresponds to an attractive interaction in the $\eta\pi^0$ P wave channel. However, the data do not require the phase of the P wave to increase over 90° nor is there compelling evidence for the intensity of the P wave to have a resonance shape in the mass range studied, i.e., from threshold to 1.8 GeV.

Mass-dependent fits, restricted to the P_+ and D_+ amplitudes and $\Delta\Phi(P_+ - D_+)$ phase difference, following the method of Ref. [11] reporting an exotic $J^{PC} = 1^{-+}$ meson decaying into $\eta\pi^-$, yield results inconsistent with those of Ref. [11] and among the three t ranges in this analysis. The discrepancy in the resonance parameters found by fitting the natural waves alone is, however, smaller than the one found by fitting the full data sample (moments).

However, by restricting the study to only P_+ , D_+ waves and the phase, $\Delta\Phi(P_+ - D_+)$, important additional information from the remaining data is ignored. For example, an exotic P wave resonance should have the same resonance parameters in all three P_- , P_0 , and P_+ waves. These waves represent different spin projections of the resonance and the data should discriminate between their production strengths.

Furthermore, we have found that the intensity of the weak waves, i.e., P and S wave above the a_0 region are more affected by leakage from the strong, D waves due to the a_2 than are the phase differences. Thus, since the mass-dependent fit to the natural waves alone, is strongly constrained by the intensity distribution of the P wave, it tends to follow the a_2 line shape, and force the fit to mimic a P -wave resonance with mass near the a_2 mass.

In a separate paper we will present an alternative description of the mass dependent P -wave amplitude and phase that does not require the existence of an exotic meson but is consistent with $\eta\pi$ rescattering.

ACKNOWLEDGMENTS

The authors wish to thank the members of the MPS group at BNL as well as the staffs of the AGS and BNL. This work was supported in part by the National Science Foundation and the U.S. Department of Energy.

[1] References from Crystal Barrel for the glueball at 1500 MeV.
[2] N. Isgur and J. Paton, Phys. Rev. D **31**, 2910 (1985).
[3] MILC Collaboration, C. Bernard *et al.*, Phys. Rev. D **56**, 7039 (1997).
[4] F. de Viron and J. Ewysers, Nucl. Phys. **B185**, 391 (1981).
[5] T. Barnes and F.E. Close, Phys. Lett. **116B**, 365 (1982).
[6] R. Jaffe, Phys. Rev. D **15**, 267 (1977).
[7] G.S. Adams *et al.*, Phys. Rev. Lett. **81**, 5760 (1998).
[8] S.U. Chung *et al.*, Phys. Rev. D **65**, 072001 (2002).
[9] E.I. Ivanov *et al.*, Phys. Rev. Lett. **86**, 3977 (2001).
[10] D.R. Thompson *et al.*, Phys. Rev. Lett. **79**, 1630 (1997).
[11] S.U. Chung *et al.*, Phys. Rev. D **60**, 092001 (1999).
[12] A. Abele *et al.*, Phys. Lett. B **423**, 175 (1998).

[13] A. Abele *et al.*, Phys. Lett. B **446**, 349 (1999).
[14] D. Alde *et al.*, Phys. Lett. B **205**, 397 (1988).
[15] Yu. Prokoshkin and S.A. Sadovskii, Phys. Part. Nucl. **58**, 606 (1995).
[16] G.M. Beladidze *et al.*, Phys. Lett. B **313**, 276 (1993).
[17] H. Aoyagi *et al.*, Phys. Lett. B **314**, 246 (1993).
[18] J. Gunter *et al.*, Phys. Rev. D **64**, 072003 (2001).
[19] S. Teige *et al.*, Phys. Rev. D **59**, 012001 (1999).
[20] Z. Bar-Yam *et al.*, Nucl. Instrum. Methods Phys. Res. A **386**, 235 (1997).
[21] T. Adams *et al.*, Nucl. Instrum. Methods Phys. Res. A **368**, 617 (1996).
[22] R.R. Crittenden *et al.*, Nucl. Instrum. Methods Phys. Res. A **387**, 377 (1997).

- [23] J. Gunter, Ph.D. thesis, Indiana University, 1997.
- [24] R. Lindenbusch, Ph.D. thesis, Indiana University, 1997.
- [25] S.U. Chung, Phys. Rev. D **56**, 7299 (1997).
- [26] E. Barrelet, Nuovo Cimento A **8**, 331 (1972).
- [27] Particle Data Group, K. Hagiwara *et al.*, Phys. Rev. D **66**, 010001 (2002).
- [28] C. Amsler *et al.*, Eur. Phys. J. C **23**, 29 (2002).
- [29] A.C. Irving and R.P. Worden, Phys. Rep. **34**, 117 (1977).
- [30] A.C. Irving and C. Michael, Nucl. Phys. **B82**, 282 (1974).
- [31] S.A. Sadovsky, Nucl. Phys. **A655**, 131c (1999).